Investigating Human Cell Influence on the Micromechanical Environment of a 3D-Printed Bone Tissue Model

Edward Alex Shangin

Thesis submitted to the faculty of the Virginia Polytechnic Institute and State University
in partial fulfillment of the requirements for the degree of

Master of Science
In
Biomedical Engineering

Caitlyn J. Collins, Chair
L. Monét Roberts
Abby R. Whittington

May 8, 2025
Blacksburg, VA

Keywords: Bone, Osteoblasts, Breast Cancer, Metastasis, Extracellular Vesicles, Tissue Engineering

Investigating Human Cell Influence on the Micromechanical Environment of a 3D-Printed Bone Tissue Model

Edward A. Shangin

ABSTRACT

Advanced stages of breast cancer (BC) are associated with the spread of tumors to distant sites, or metastasis, with the skeletal system being one of the most common locations for metastasis, with rates as high as 70%. Despite this, the mechanistic factors behind BC cell recruitment, infiltration, and survival in the bone niche remain underexplored. Extracellular vesicles (EVs) are membrane-bound particles that facilitate intercellular communication between cancer and bone cells to form pre-metastatic niches, infiltrate tissue systems, and promote survival. Current models, such as 2D in vitro cell culture and preclinical animal models, fail to replicate the physiological metastatic bone environment, leading to high failure rates of anti-cancer drugs and limited predictive accuracy. This study aims to enhance a previously developed 3D-printed bone tissue culture model to mimic the human bone microenvironment by seeding osteoblasts to assess metastatic mechanisms and the influence of breast cancer cell lines on in vitro model mechanical properties, in breast-to-bone metastasis.

Dynamic mechanical analysis (DMA) was conducted on osteoblast-seeded scaffolds (n = 24) across 7-, 14-, and 21-day timepoints to assess changes in storage modulus, loss modulus, and damping coefficient (tanδ). SEM was used to evaluate cell adhesion, mineral deposition, and scaffold degradation, while μCT characterized porosity, strut thickness, and trabecular separation after long-term culture.

To assess the metastatic influence of breast cancer extracellular vesicles (EVs), viability and proliferation assays were performed to optimize co-culture conditions and

evaluate EV effects on osteoblast growth. Co-cultured scaffolds with human osteoblasts and T47D cells were analyzed by DMA at 4 and 7 days to assess mechanical changes, and osteocalcin ELISA was used to examine alterations in bone-specific protein expression.

Voronoi scaffolds exhibited a decrease in stiffness over time, while TO scaffolds remained stable; Voronoi scaffolds maintained a significantly higher storage modulus ($p = 0.038$). SEM and μCT confirmed qualitative mineralization and degradation, along with scaffold print fidelity (i.e., Trabecular Separation = 521 μm), respectively. Co-cultured scaffolds showed a non-significant increase in both stiffness and osteocalcin expression. Together, these results support the use of this platform for modeling bone tissue in vitro as well as metastatic mechanisms in breast-to-bone cancer progression.

Investigating Human Cell Influence on the Micromechanical Environment of a 3D-Printed Bone Tissue Model

Edward A. Shangin

GENERAL AUDIENCE ABSTRACT

Late stages of breast cancer (BC) are linked with the spread of tumors to distant sites, or metastasis, with the skeletal system being one of the most common locations, affecting up to 70% of patients. Despite this high prevalence, the mechanistic factors behind BC cell recruitment, infiltration, and survival in the bone niche remain underexplored. Extracellular vesicles (EVs), membrane-bound particles, communicate between cancer and bone cells to help form pre-metastatic niches, penetrate tissue systems, and promote cancer cell survival. Current preclinical models, such as 2D in vitro cultures and animal models, fail to replicate the physiological environment of the metastatic bone niche, leading to limited predictive accuracy and high anti-cancer drug failure rates. To address this gap, this study enhances a previously developed 3D-printed bone tissue culture model by seeding bone cells to better mimic the human bone microenvironment and evaluate both metastatic mechanisms and mechanical responses of breast cancer cells during bone colonization.

Dynamic mechanical analysis (DMA) was performed on bone cell-seeded scaffolds (n = 24) at 7-, 14-, and 21-day intervals to monitor changes in stiffness (storage modulus), energy dissipation (loss modulus), and damping behavior (tanδ). SEM was used to examine cell attachment, mineral deposition, and scaffold breakdown, while microcomputed tomography (μCT) characterized porosity, strut thickness, and pore diameter following extended culture.

To assess the metastatic influence of breast cancer-derived EVs, viability and proliferation assays were performed to identify ideal co-culture conditions and quantify EV effects on osteoblast growth. DMA was repeated on co-cultured scaffolds (bone and BC cells) at 4 and 7 days, and osteocalcin ELISA was used to measure changes in bone-specific protein expression.

Voronoi scaffolds exhibited a time-dependent decrease in stiffness, while Truncated Octahedron (TO) scaffolds remained mechanically stable; however, Voronoi scaffolds consistently showed a significantly higher storage modulus ($p = 0.038$). SEM and μCT confirmed mineral deposition, scaffold breakdown, and print fidelity (pore diameter = 521 μm). Co-cultured scaffolds showed a non-significant increase in both stiffness and osteocalcin expression. Together, these findings support the potential of this platform to model and assess key mechanisms of breast-to-bone cancer metastasis.

DEDICATION

This thesis is dedicated to my parents, Natallia and Georgiy, and my sister, Liza, who have deeply and lovingly supported me through every step of my strenuous academic journey. Thank you, Edward

ACKNOWLEDGEMENTS

First and foremost, I would like to extend my most heartfelt gratitude to Dr. Caitlyn Collins for welcoming me into her lab and opening a new avenue in my research career. Her passion for bone research inspired me to pursue tissue engineering for my master's degree. Thank you for your invaluable mentorship and unwavering support from the very beginning of my journey.

I would also like to sincerely thank my committee members, Dr. L. Monét Roberts and Dr. Abby Whittington, for their expertise and guidance in helping me refine my research focus and complete my thesis.

Additionally, I am grateful to De Shanna Johnson for her assistance and guidance on the breast cancer aspect of my thesis and to Zahra Bahranifard for her help with the scaffold manufacturing for my thesis. I extend my deepest appreciation to Hannah Marrone, the exceptional undergraduate student I had the privilege of mentoring. Her enthusiasm, curiosity, and willingness to lend a helping hand made her an indispensable research assistant and a joy to work alongside.

Finally, I could not have completed this academic journey without the physical and emotional support of my lab mates and friends. Their efforts in fostering a collaborative, safe, and joyful lab environment made this experience truly enjoyable. To my friends back home, your constant encouragement to persevere and continue making an impact in science has meant the world to me. I am incredibly thankful for the memories we have created and the support I received in and out of the lab.

Figure List

Table List

Table of Contents

1 Chapter 1: Introduction

1.1 Background

Breast cancer (BC) is the most commonly diagnosed amongst all cancers, with over 2 million women globally being diagnosed and another 670,000 succumbing to this disease annually[1]. Advanced stages of BC are associated with the spread of tumors, with the skeletal system being one of the most common locations for metastasis, with rates as high as 70%[2]. Factors contributing to preferential breast-to-bone metastasis are poorly understood, with the role of circulating cells, such as extracellular vesicles, being hypothesized as a significant contributor[3]. Similar to all cells, breast cancer cells secrete extracellular vesicles (EVs). EVs have been noted as contributing to metastatic mechanisms such as homing, where EVs serve as mediators for intercellular communication and establishing the pre-metastatic niche[4,5]; extravasation and infiltration, where EVs disrupt endothelial barriers to allow breast cancer cells to invade the tissue[6]; and survival and proliferation, where EVs from tumor cells can alter turnover and grow rapidly[7,8]. Despite knowing these mechanistic factors behind BC, the underlying impact of EVs in cell recruitment, infiltration, and survival in the bone niche remains underexplored. Current preclinical models, such as 2D in vitro cell culture and preclinical animal models, fail to spatially replicate the metastatic bone environment and neglect the cancer progression, leading to underrepresented modeling. However, recent advancements in 3D printing have enabled the fabrication of *in vitro* models that have the potential to mimic the bone micromechanical environment. As such, there is a need to explore 3D *in vitro* models to replicate the metastatic niche and better understand the mechanisms associated with metastasis and mechanically characterize the co-culture environment.

1.2 Motivation

This study aims to enhance a previously developed 3D-printed bone tissue culture model to 1) mimic the human bone microenvironment by seeding human osteoblasts (1.19 hFOB, ATCC) for extended culture *in vitro* studies and 2) apply the bone tissue culture model to assess the role of EVs in the recruitment and survival of three metastatic breast cancer cell lines, MDA-MB-231, MDA-MB-468 and T-47D, in breast-to-bone metastasis. To progress the existing bone tissue culture model to serve as a bone *in vitro* model, we must be able to physiologically simulate bone proliferation, extracellular matrix formation, and mechanical properties to recapitulate the bone niche.

1.3 Introduction of Aims and Hypothesis

1.3.1 Research Aim 1

My first aim is to characterize extracellular matrix formation (ECM) and maturation in an *in vitro* bone tissue culture model seeded with human osteoblasts (1.19 hFOB) using modalities like scanning electron microscopy (SEM), confocal imaging, microcomputed tomography (μCT), and dynamic mechanical analysis (DMA).

Hypothesis

Long-term static culture of human osteoblasts, compared to murine fibroblasts, will better mimic the natural bone microenvironment, resulting in elevated mineral deposition and increased mechanical properties from mature hOBs determined by imaging modalities and DMA.

Approaches and Outcomes:

3D scaffolds (Fig. 1.1, 1 cm^3 geometries) with complex (random) and repeating unit cell microarchitectural geometries, Voronoi and Truncated Octahedron (TO), respectively, will be manufactured using vat photopolymerization and a novel, osteogenic photopolymer resin made of 50 wt.% epoxidized soybean oil acrylate (ESOA) and 50 wt.% PEGDA (provided in collaboration

with the Whittington Lab at Virginia Tech). The scaffolds will be seeded with human osteoblast cells (hFOBs, ATCC, 2.5×10^4 cells/ scaffold) and cultured for 7, 14, and 21 days under static conditions. Confocal microscopy will confirm cell adhesion and proliferation and analyze cell distribution. μCT and SEM imaging will assess the ECM formation and mineral deposition. After culturing, DMA will be utilized to determine changes in mechanical properties with culture time. A strain sweep with a dynamic amplitude (DA) starting at 0.2 mm (2% strain) and gradually increasing to 1 mm (10% strain) at a constant step size of 0.1 mm at a frequency of 0.1 Hz will be applied. Mechanical parameters like storage modulus (E'), loss modulus (E"), and energy dissipation (tanδ) will be recorded. Storage modulus data is of interest due to the interpretation of how cell culture time impacts the viscoelastic mechanical properties of the scaffold. From this study, we will use a previously developed mechanical protocol to enable cross-comparison to published work and establish a multi-modal imaging protocol to determine optimal culture times and conditions for recreating the bone microenvironment.

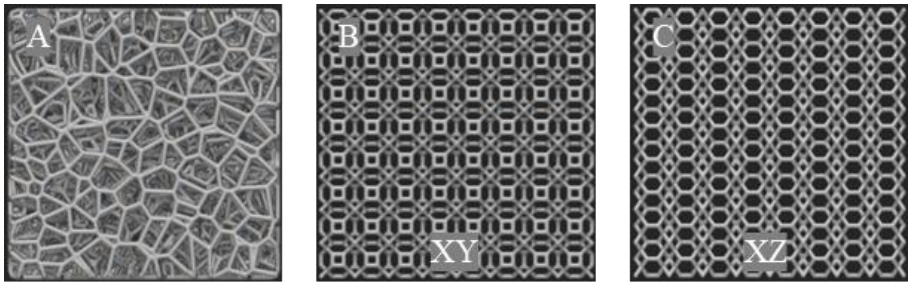

Figure 1. Ideal CAD geometries. A) Voronoi, B-C) TO structures are provided by the Whittington lab.

1.3.2 Research Aim 2

My second aim is to characterize the impact of extracellular vesicles (EVs) on the recruitment, infiltration, and survival of breast cancer cells in the bone niche. In addition to preliminary studies establishing culture conditions and 2D bone cell culture response to EVs, scaffolds from Aim 1 will be co-cultured with T47D breast cancer cells and mechanically characterized to determine the mechanical properties of a tumor-infiltrated bone model.

Hypothesis

Introducing breast cancer-derived EVs into co-culture with human osteoblasts is expected to improve osteoblast proliferation and cell viability. Consequently, co-culturing breast cancer cells with osteoblasts will result in increased mechanical characteristics and upregulation of expression of osteoblast-specific biomarkers.

Approaches and Outcomes

To understand the mechanisms of breast cancer-derived EVs on the survival and proliferation of osteoblast cells in the bone niche, 1.19 hFOBs will be 2D co-cultured with cancerous and non-cancerous breast cell line-derived EVs. This study will analyze extracellular vesicles from two triple-negative breast cancer (TNBC) cell lines (MDA-MB 231 and MDA-MB 468), an estrogen receptor-positive (ER+) cell line (T47D), and a non-cancerous breast tissue cell line (MCF10A). Osteoblasts will be cultured in different concentrations of breast cancer and osteogenic media to establish an ideal culture condition for bone and breast cell co-culture applications. Human osteoblasts will then be exposed to cancerous and non-cancerous breast cell-derived EVs to investigate their effects on bone cells. Finally, to explore the applicability of the bone tissue culture model for *in vitro* studies of breast-to-bone metastasis, scaffolds from Aim 1 will be co-cultured with T47D breast cancer cells and 1.19 hFOBs to characterize the environment mechanically. Through this preliminary *in vitro* modeling, data will be collected to enable optimization of the scaffolds from Aim 1 for future studies targeting infiltration and recruitment mechanisms of breast-to-bone metastasis.

2 Chapter 2: Literature Review

This chapter presents an in-depth literature review of foundational topics relevant to my thesis. Specifically, it examines literature on bone physiology and mechanics, existing *in vivo* and *in vitro* bone models, breast cancer physiology, and *in vitro* breast-to-bone models.

2.1 Bone Physiology and Mechanics

Bone Physiology

The bone is a dynamic, multicomponent organ that provides several key functions to the human body. These functions include driving locomotion through muscle attachment, providing structural support, protecting vital organs, regulating blood and storing essential minerals, and serving as an endocrine organ[9–12]. Bone is the central component of the musculoskeletal system, a complex structure comprised of bones, muscles, tendons, ligaments, and cartilage[13], and accounts for roughly 15% of the total human body weight[14,15]. Although bones are composed of several tissue types, the two macroscopic osseous tissues, cortical and trabecular bone, are of interest.

When looking at bone, the visible layer is the compact bone tissue, also known as cortical bone. Cortical bone is the dense, outer layer of bone that accounts for approximately 80% of the bone mass in the adult skeleton and serves as a protective layer for the internal cavity. Cortical bone tissue is highly resistant to mechanical loading, particularly bending and torsion[15,16]. Its dense, rigid structure is essential for providing structural integrity and supporting high mechanical loads. Due to its role in weight-bearing and its resistance to deformation, the porosity of the tissue is relatively low (3-5%[15,17]), allowing it to maintain strength and stiffness under stress. Covering the cortical bone is the periosteum, a thin, membranous, double-layered structure that plays roles in bone cell remodeling, nutrient delivery, and supplying sensory nerves for pain detection[16,18,19]. Its two layers consist of a fibrous outer layer and an inner cambium layer, which is more cellular

and vascular [20]. The fibrous outer layer is an irregular, dense connective tissue made primarily of elastic material like collagen, and interacts with tendons, ligaments, and muscles[21]. The cambium layer, also known as the osteogenic layer, is made up of mesenchymal progenitor cells, differentiated osteogenic progenitor cells, young osteoblasts, and fibroblasts[21,22], all of which are crucial for bone formation. Osteons are the basic building block of cortical bone and can be divided into primary and secondary osteons[23]. Primary osteons are located adjacent to the cortical shell and near blood vessels, surrounded by an organized collagen fiber membrane called the concentric lamellae (5-7 µm)[24,25]. Secondary osteons, or the Haversian system, form a cylindrical structure of lamellae around blood vessels called a Haversian canal (~400 mm long and 200 mm wide at their base)[24,26]. Since cortical bone has less metabolic activity than trabecular bone, these canals are essential to ensure that nutrients and sensory information are properly transferred to osteocytes to facilitate communication during remodeling. The structure of cortical bone is represented in Figure 2.

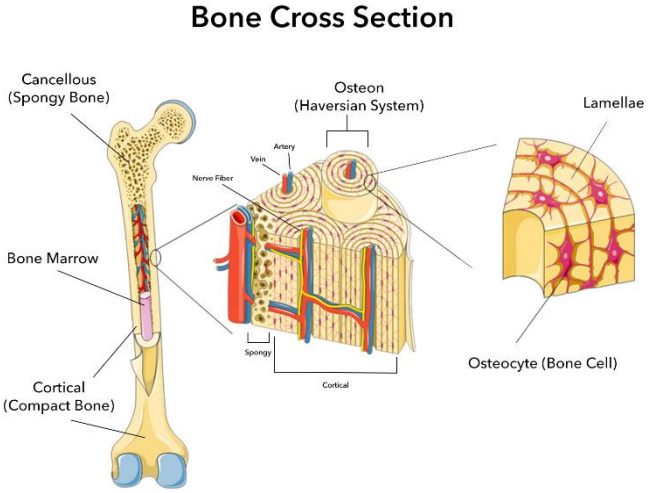

Figure 2. Cross-sectional segment of cortical bone components (adapted from [27])

When looking at the cross-section of the bone, cancellous, or trabecular, bone tissue is exposed, which accounts for approximately 20% of the remaining bone mass in an adult. Unlike cortical bone, trabecular bone is highly porous (40-95%[17]), adopting a honeycomb-like structure

as shown in Figure 3. Trabeculae are found primarily in the proximal and distal ends of long bones and are encapsulated under cortical bone[9]. Trabecular bone tissue is less calcified and has a larger surface area than cortical bone, which enables pronounced metabolic activity and allows for higher bone turnover and resistance to strain (50%)[26,28,29]. The basic structural units of trabecular bone are known as hemi-osteons, or bone packets. Trabecular bone is made up of spicules and rods (trabeculae), which average 50 to 400 mm in thickness[26] and provide internal structural strength and housing to osteocytes[25]. Lamellae layers also contribute to trabecular bone structure, with their layers oriented in slightly varying directions to form the characteristic, lattice-like structure[25]. The high metabolic rate and presence of osteocytes in trabecular bone play critical roles in bone remodeling, as mechanical deformation sensed by osteocytes can trigger the remodeling process[30]. The continuous remodeling due to mechanical loading or osteoclast breakdown triggers osteoblasts in the trabeculae to build osteoid, which are collagenous structures of extracellular matrix (ECM) that mineralize into newly formed lamellae layers[27]. Replicating the intricate architecture of trabecular bone *in vitro* can pose a challenge, but it is essential for developing accurate models and advancing our understanding of bone formation mechanisms.

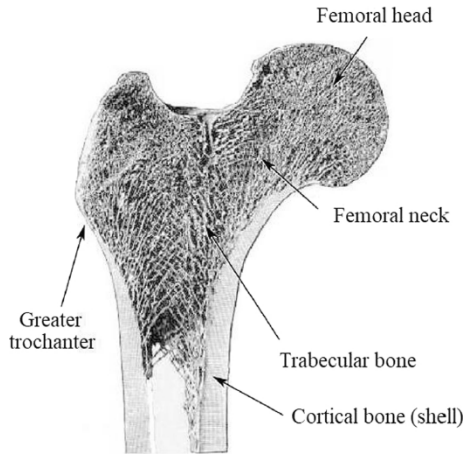

Figure 3. Cross-sectional segment of trabecular bone (adapted from [31])

Cortical and trabecular bone tissue are similar in composition, as both serve as reservoirs for calcium and other essential minerals. They are both comprised of inorganic mineral

(hydroxyapatite, 70%), organic proteins (collagen, 20%), and water (10%)[32–34], as shown in Figure 4. The organic matrix of bone is comprised primarily of collagen type I, which accounts for 90% of the total collagen content, with smaller amounts of collagen types III and V also present. The remaining 10% consists of non-collagenous (NCPs), which play crucial roles in regulating collagen formation, mineralization, and fibril size[32].

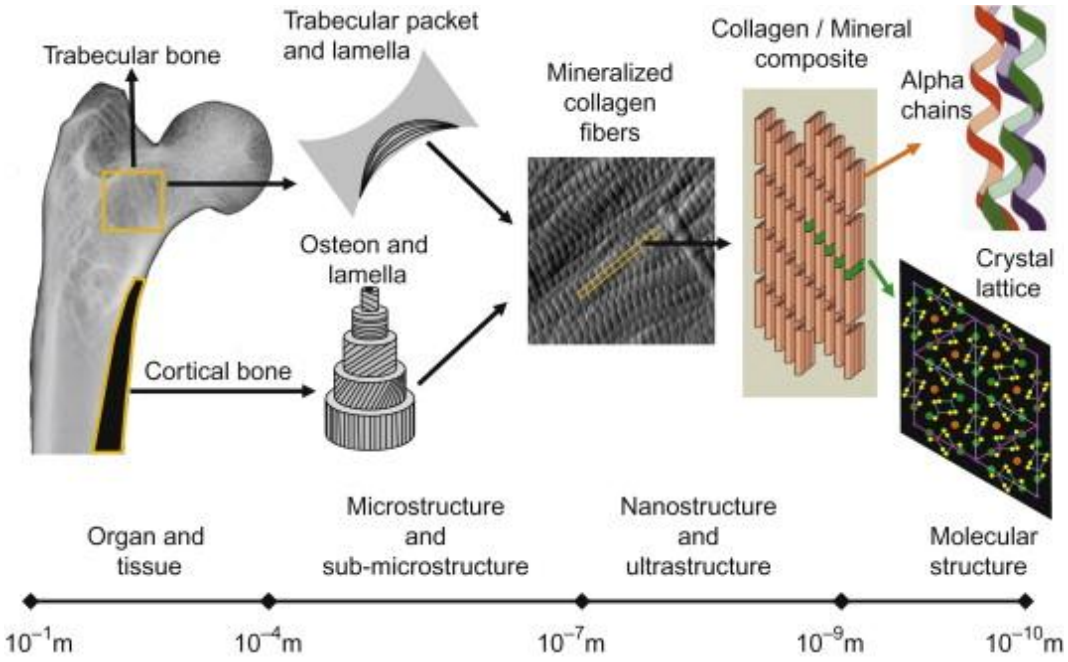

Figure 4. Schematic of the bone microscopic hierarchy (adapted from [32])

Cell Physiology and Bone Remodeling

Bone is inherently a highly complex tissue composed of multiple layers and specialized structures. Bone remodeling, healing, and maintaining structural integrity are driven by four different types of bone cell types: osteoclasts, osteoblasts, osteocytes, and bone lining cells[35]. Each cell type has an essential function in ensuring bone homeostasis (Figure 5).

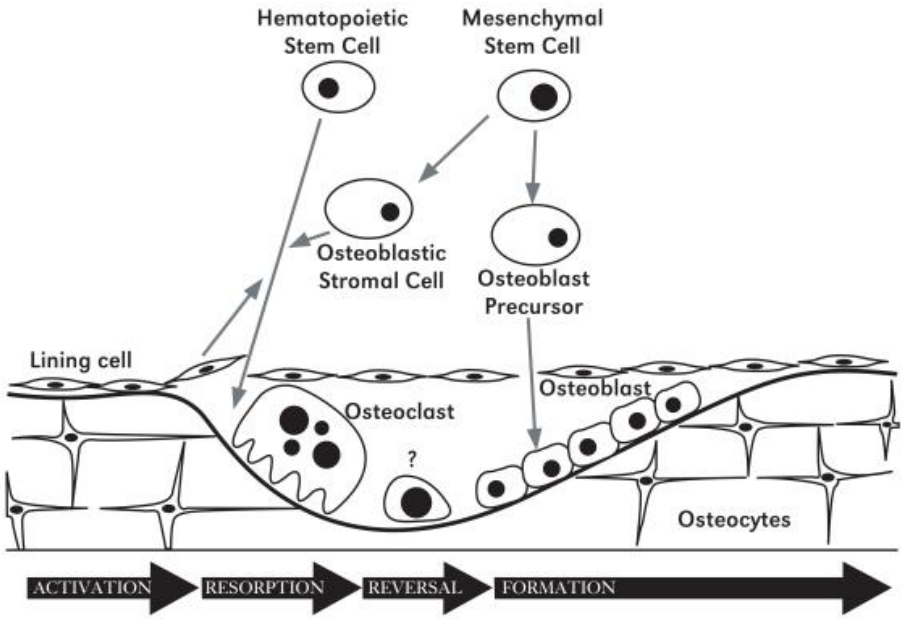

Figure 5. Sequence of bone remodeling cells (adapted from [11])

Osteoclasts are a multi-nuclei cell type with a high metabolic state, a vital feature for bone remodeling. Osteoclasts' primary function in remodeling is to break down or resorb bone tissue. The ruffled border, a folded membrane in the osteoclast cytoplasm that forms microvilli-like ridges at the bone surface, is where resorption takes place[35]. The process of acidification and transcytosis is the driving process at which inorganic material is dissolved and then removed as degraded products, respectively[36]. Osteoclasts have integrins, which are cell adhesion molecules that attach to localized organic extracellular matrices like collagen, osteopontin, and bone sialoprotein[35].

Osteoclasts originate from hematopoietic stem cells, making them part of the macrophage family[35]. Hematopoietic stem cells differentiate into mononuclear osteoclast precursors when exposed to macrophage colony-stimulating factor (M-CSF). These precursors express RANK receptors which bind to RANKL, a key osteoclastogenic protein, triggering their differentiation and fusion into assembled multinucleated osteoclasts. Full maturation occurs when these osteoclasts interact with osteoblast-lineage cells[35,37].

Unlike osteoclasts, osteoblasts are mononuclear cells characterized by an enlarged Golgi apparatus and prominent rough endoplasmic reticulum, which reflect their role in creating and secreting bone matrix, essential for bone remodeling[37]. Opposed to osteoclasts, the primary function of osteoblasts is to form and store new bone matrix. Bone formation is a two-step process where osteoblasts produce unmineralized osteoid, which is then mineralized to hardened crystals. Osteoid is comprised of 90% collagen and 10% non-collagenous proteins, which undergo post-translational modifications such as hydroxylation, glycosylation, and phosphorylation to regulate collagen stability, extracellular matrix organization, and mineralization[38]. As osteoblasts move, exposed osteoid starts to mineralize into hydroxyapatite crystals, transforming them into rigid calcified bone matrix[39]. Once osteoblasts have formed new bone matrices, they may become embedded as osteocytes in the mineralized bone matrix, differentiate into bone-lining cells, or undergo cell apoptosis.

Osteocytes make up 90-95% of the total bone cell population and have a lifespan of up to 25 years[40]. Once osteocytes differentiate from osteoblasts, they embed themselves into an ellipsoidal space called the lacunae, which is surrounded by bone matrix[41]. Within their lacunae, osteocytes exhibit a branching, dendritic morphology, extending cellular processes through small channels called canaliculi. These processes connect with neighboring osteocytes, enabling cell-cell communication. Due to functional adaptations within the bone regarding mechanical loading, nutrient transport, and mechanosensing across the bone matrix, osteocytes present different morphologies in cortical and trabecular bone; in cortical bone, osteocytes present a dendritic morphology, whereas in trabecular bone, they appear more rounded[40,42]. Osteocytes do not have a definitive function, but contribute significantly to localized and systemic mineralization regulation, sensing mechanical loading, bone homeostasis, and endocrine signaling[41,43,44]. For an

osteocyte to fully mature into a mineralized bone cell, osteoblast markers like osteocalcin, bone sialoprotein II (BSPII), collagen I, and alkaline phosphatase (ALP) are downregulated[40]. Meanwhile, markers like non-collagenous protein and glycoprotein, DMP1, and sclerostin are upregulated. Therefore, an *in vitro* model that aims to recapitulate mature bone should demonstrate a similar shift in gene and protein expression to ensure the presence of functionally mature osteocytes.

Bone Mechanical Properties

Cortical bone is known to shield trabeculae by resisting deformation and sustaining high mechanical loads, but there is evidence that trabecular bone plays an equally influential role in maintaining mechanical integrity by distributing load to the cortical shell[45].

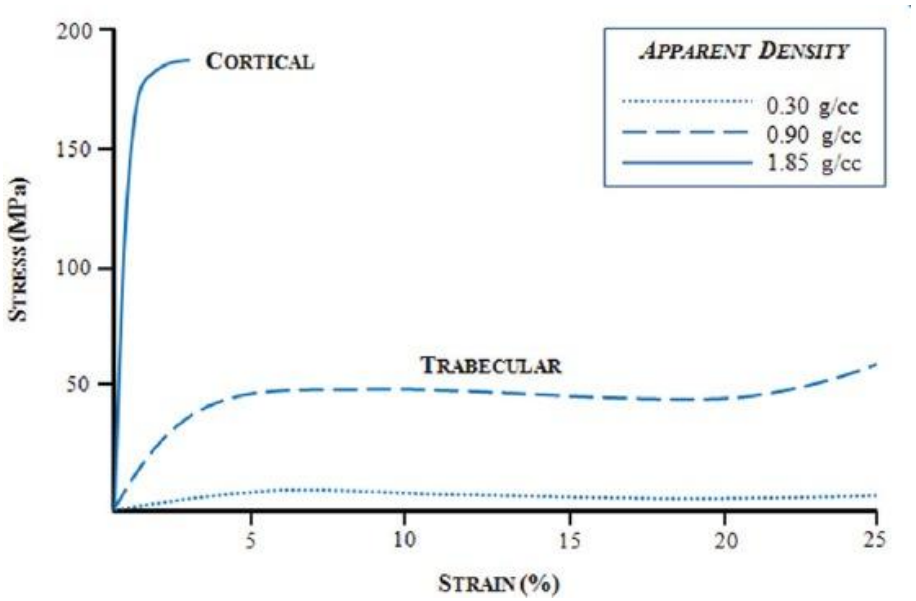

Figure 6. Compression stress-strain curve of macroscopic bone tissue at different densities (adapted from [28,46])

Trabecular bone is the prominent load-bearing tissue in vertebral bodies and aids in transferring load from joints to cortical bone in long bones[47]. As previously mentioned, trabecular bone has higher metabolic activity compared to cortical bone, rendering it more likely to undergo frequent remodeling. Trabecular bone outperforms cortical bone in compression, maintaining relatively high stiffness at high levels of strain (Figure 6). However, trabecular bone performs

poorly in tension and exhibits the lowest strength in shear. It is also highly susceptible to profound changes in density with aging, as much as a 10% decrease per decade[47]. Due to the time-dependent, heterogeneous, and anisotropic nature of trabecular bone, it is challenging to predict its mechanical properties using standard mechanical testing methods[47]. Its viscoelastic behavior is influenced by several parameters such as loading direction, anatomical site, and porosity[47]. These complexities hinder the development of accurate *in vitro* bone models that recapitulate the bone micromechanical niche. For my thesis, I will be specifically targeting trabecular and osteoid/early ECM tissue mechanics. Prior investigations have confirmed that our osteoconductive scaffold successfully replicates key features of the bone microenvironment[48].

2.2 In Vivo and 3D In-Vitro Models

In Vivo Models

To assess the effects of new therapeutics or clinical applications on bone tissue, *in vivo* animal models are typically used to mimic human physiology as closely as possible. Rodents, rabbits, canines, pigs, ruminants, and nonhuman primates (NHPs) are currently being used for different bone research applications, including fracture healing, implants, cancer metastasis, and osteoporosis[49,50]. Rodents are cost-effective and have high levels of genetic similarity to humans; however, drastically different body masses, bone healing rates, long bone compositions, and differences in mechanical loading mechanisms render rodents incapable of fully replicating the healing process of human bone[51,52]. Rabbits have bone density that closely resembles that of human bone and similarly undergo advanced stages of secondary osteonal remodeling, but healing times vary and are more robust than human bones[52,53]. Canine bone has many similarities to human bone, which include the formation of secondary osteons, analogous intracortical remodeling activity, and age-associated bone loss[52,54]; however, limitations include significant variance in the remodeling and apposition rates within and between dog breeds, low estrous cycles, and specimen availability

due to social and ethical pressures[54]. Pigs share similar bone mineral density, anatomy, morphology, remodeling capability, and bone regeneration rate with humans[52,53], however, they have a lower biological resemblance to humans due to their excessive body weight and relatively short long bones. Of the most common preclinical animal models, NHPs are the most genetically similar to humans, go through osteonal remodeling, and develop similar bone-related diseases such as osteoarthritis, age-related bone loss, and postmenopausal osteoporosis[54]. NHPs are relatively costly, however, pose ethical considerations, and have shorter long bones than humans do. Ruminants are the most clinically relevant preclinical animal model due to their docility and their comparable body weight, bone size, and healing potential to humans. Sheep typically undergo seasonal bone loss, which can be compared to age-related bone loss in humans[54]. The use of animal models has its advantages, but cell-based methods, such as *in vitro* models, can replicate the human bone microenvironment without requiring the use or sacrifice of animals, rendering it a safer, more ethical alternative for studying human disease.

In Vitro Models

I will be focusing on exploring the bone microenvironment via *in vitro* models that mimic bone structure and micromechanical environment. *In vitro* models involve experiments that take place outside of a living organism. These models are considered more ethical compared to *in vivo* models, but successfully reproducing an organ system is challenging due to the intricacies and complexities of the overarching system. 2D *in vitro* bone models are typically used as a pre-screening tool and include conventional 2D culture, sandwich culture, micro-patterning, and altering substrate stiffness[55]. Traditional 2D cultures are commonly used to identify suitable osteoblast cell types for cell culture. Sandwich cultures are sometimes considered a 3D model, where cells of interest are cultured in-between two extracellular matrix layers and used to assess

pharmacokinetic effects[55]. The ability of sandwich models to accurately simulate the bone microenvironment warrants further investigation; however, since it is a relatively new technique, there is an insufficient amount of data using human osteoblasts for this model to make conclusions on its suitability as a fidelic bone tissue model[55]. Alternative *in vitro* 2D+/3D tissue modeling approaches, such as micro-patterning and alternating substrate stiffness modeling utilize modified substrate tomography to include different surface textures (grooved and rough), porosities (150-500 microns), and stiffnesses (4,7 MPa) for characterizing the bone microenvironment and assess bone cell differentiation[56,57]. A study conducted by Ball et. al used alternating substrate stiffness modeling and found that osteoblast behavior is dependent on surface roughness and material properties[58]. Such 2D *in vitro* culture models can serve well as preliminary studies but ultimately fail to represent the complex interactions between cell lines and the 3D nature of the bone microenvironment.

3D *in vitro* models with intricate microstructure play a critical role in effectively replicating the complexity of a human organ system. These models can use patient-specific cell lines for applications such as fracture healing and metastatic mechanisms[59]. A variety of 3D *in vitro* models have been developed for human tissues, including spheroids, hydrogels, and scaffolds[56]. Spheroids are useful in modeling cell-cell and cell-matrix interactions. They can also be used for microfluidic device development, collagen gels, and hanging drop culture[60]. Generally, spheroids are effective at replicating gene expression, morphology, and viability, but lack porosity structures and tissue mechanical properties due to suspension in a liquid medium[55]. Hydrogels more closely represent the 3D nature of the bone microenvironment since they are created using natural polymers such as collagen or gelatine[61]. However, hydrogels are known to sustain poor cell proliferation and inadequate matrix deposition, which may lead to progressive degradation, potentially altering

mechanical properties[55,56]. These limitations make hydrogels less suitable for bone regeneration research in translational and clinical applications. Scaffolds are similar to hydrogels in that they provide 3D matrix support for cell growth and regeneration but also allow for more convolution when fabricating models. A complex 3D environment can be created from scaffolds to mimic the porosity and mechanical properties of bone. Scaffolds are also versatile with regard to manufacturing; they can be made out of several different materials (metal, polymers, natural materials) and manufactured using a multitude of techniques (electrospinning, 3D printing, and leaching)[48,62]. Overall, scaffolds offer the most effective capability of replicating the bone niche and can be implemented across numerous bone-related and clinical application studies[63,64].

Although 3D *in vitro* modeling of bone presents a unique challenge, recent work has made significant advances in developing biofidelic 3D bone tissue models. A study conducted by Olevsky et al. uses both 3D printing and leaching techniques to create a plastic gyroid lattice and chitosan-gelatin cryogel scaffold to replicate the bone microenvironment[65]. This study was able to successfully create a novel scaffold by incorporating two different techniques; however, there were some limitations. The combined scaffold exhibited decreased elasticity and swelling capacity and became more cytotoxic with additional resin. To account for this, future studies should explore different 3D materials to increase biocompatibility and bone cell differentiation[65]. Another study conducted by De Leeuw et al. created a pipeline to develop a 3D printed human bone-derived cell-laden scaffold to explore the effects of cell density on matrix formation, stiffness, and cell morphology[66]. Their study successfully developed a scaffold that saw an increase in mineral density and stiffness with more physiological cell density[66]. However, due to the pilot nature of this study, isolated cells were from one donor, and non-homogeneous populations may have been collected. Since there was no presence of a co-culture environment, the recapitulation of the

complex microenvironment was not fully complete, and limited collagen formation was observed[66]. Future studies should assess increased cellular complexity to ensure the bone microenvironment is entirely reproduced.

2.3 Breast Cancer

Physiology, Epidemiology, and Risk Factors

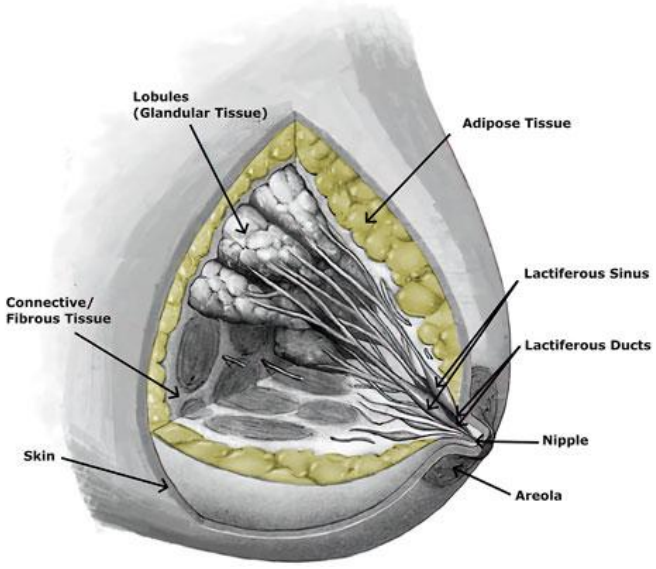

Figure 7. Anatomy of the breast (adapted from [67])

Breast cancer is a malignant disease characterized by abnormal cell growth in breast tissue that primarily affects females but can be diagnosed in both male and female populations[68]. The breast can be broken up into three parts: the milk-producing lobule glands, ducts for transport, and connective tissue, which is made up of both fibrous and fatty structures. The lobule glands and ducts are the most common locations for abnormal breast cell growth. As of 2020, female breast cancer has surpassed lung cancer as the most commonly diagnosed cancer globally, accounting for 11.7% of all cancers diagnosed, with an estimated 2.3 million new cases annually[69]. Globally, breast cancer accounts for approximately one-third of all malignancies in women, with a mortality rate of 15%[70]. Both non-modifiable and modifiable risk factors play roles in breast cancer development. Non-modifiable risk factors involve demographics such as sex, age, race or ethnicity, genetics, and menstrual period and menopause characteristics[71]. Black women have a

higher proportion of distant-stage cancer compared to women of other races, making them twice as likely to develop hormone receptor (HR) and human epidermal growth factor receptor 2 (HER2) negative tumors (19%)[72]. Modifiable factors, those that can be prevented or moderated to decrease the likelihood of breast cancer, include obesity, alcohol and nicotine intake, poor diet, environmental exposure, and hormonal therapy[71]. Breast cancer is more likely to occur in women in Western and other developed countries due to the increased presence of certain modifiable factors such as environmental exposure and obesity, but the mortality rate in these countries is significantly lower than in other, less developed countries due to the advancement of early detection techniques[73].

Breast cancer can be classified as either invasive or non-invasive, depending on whether tumors or masses are benign (non-cancerous) or malignant (cancerous). Non-invasive, or *in situ* breast cancer does not spread past the initial breast tissue. *In situ* breast cancer can then be split into ductal carcinoma *in situ* (DCIS) and lobular carcinoma *in situ* (LCIS), which target regions of the milk ducts and lobules, respectively. DCIS makes up approximately 16% of all breast cancer diagnoses and is deemed a precursor to invasive breast cancer[74], which is classified by infiltration past the initial location of the tumor. Invasive ductal carcinoma (IDC) is one of the most common types of invasive breast cancer, which makes up 70 to 80% of diagnosed patients [75]. Invasive lobular carcinoma (ILC) is the second most common type of invasive breast cancer, accounting for 10% of all invasive breast cancers. For my thesis, I am investigating the mechanism of two other breast cancer types, triple-negative and estrogen receptor-positive breast cancer, whose respective cell lines will be described below.

Breast Cancer Cell Types

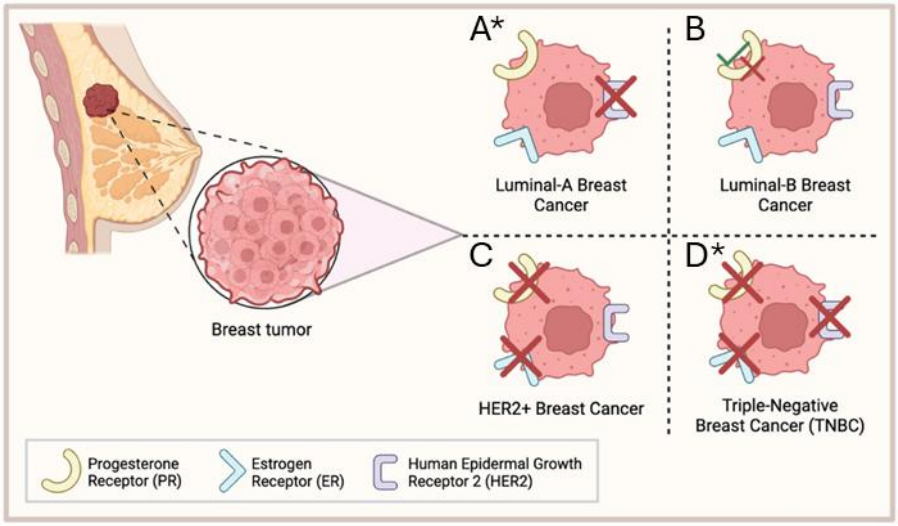

Figure 8. Visual representation of different types of breast cancer. A) T47D breast cancer; a Luminal-A subtype B) Luminal-B breast cancer C) HER2+ breast cancer D) MBA-MD-231 & 468 breast cancer; TNBC subtypes (adapted from [76]) *shows which cancer type we are investigating

Isolated from a pleural effusion of a 51-year-old white female with IDC, the MDA-MB-231 cell line is commonly used to model late-stage, triple-negative breast cancer (TNBC). The cell line can be characterized as estrogen receptor (ER), progesterone receptor (PR), E-cadherin, and HER2 protein negative, but does express a mutation in the tumor protein 53 (p53) gene[77]. The TNBC phenotype is associated with aggressive and dismal survival rates, making it the most threatening among all breast cancers[78,79]. MDA-231 cells exhibit an epithelial morphology, often appearing spindle-shaped[80], which increases its invasive potential[81].

MDA-MB-468 cells are also isolated from a pleural effusion of a 51-year-old patient with breast adenocarcinoma, a more general type of breast cancer targeting the glandular cells. Opposite to the MDA-231, MDA-468s were isolated from a black female that showed the G6PD A phenotype[82]. G6PD deficiency is caused by the absence of the enzyme G6PD, which plays a role in helping red blood cells protect against oxidative stress and NADPH production. Without G6PD, the patient becomes hemolytic anemic, a condition where red blood cells break down more quickly, leading to tachycardia, bilirubin gallstones, and enlarged hearts[83–86]. MDA-468 also

shows a mutation on p53, as well as negative expressions in ER, PR, E-cadherin, and HER2. In contrast to their counterpart, MDA-468 cells exhibit a more spherical morphology, which might play a role in their invasive characteristics[79]. Additionally, Tate et. al. observed that MDA-231, a less invasive cell line compared to MDA-MB-468, was more likely to be resistant against hyper-acetylation and DNA degradation drugs[79], making it a relevant cell line to study.

T47D is a sub-category of Luminal-A breast cancer with conditions like ER+, PR±, and $HER2^-$. Like the previous cell lines, T47D cells are also isolated from the pleural effusion of a 54-year-old with IDC. Unlike TNBC cells lines, T47D is a hormone-dependent breast cancer, meaning these cells are sensitive to estrogen receptors (ER)[87]. T47D cells also show tumorigenic properties and present mammalian epithelium characteristics, like squamous or cuboidal shape[87]. Typically, T47D cells are not as invasive compared to TNBC, but studies in recent years have shown that T47D cells exhibit distinct molecular characteristics ideal for *in vitro* modeling of progesterone-responsive Luminal-A breast cancer[87]. Holen et al. assessed breast cancer metastasis to bone and found that when nude mice with T47D tumors were supplemented with estradiol, an estrogen hormone, metastases presented within 65% of mice[88]. The T47D cells were found to have specifically invaded the tibia and femur; no evidence of metastasis elsewhere was detected[88]. Additionally, Montt-Guevara et al. identified that androgens, a group of developing and growth hormones, changed the actin cytoskeleton and increased migration and invasion, and is closely related to tumor metastasis[89]

MCF10A is an epithelial cell line isolated from a 36-year-old patient's reduction mammoplasty involving a benign fibrocystic tissue[90,91] that can be used to compare tumorigenesis of malignant cell types, TNBC, and ER+. Similar to T47D cells, MCF10A cells show a cuboidal, epithelial morphology in 2D culture and transition into spheroid structures when cultured in 3D[91].

Since the cell line comes from non-malignant tissue, it exhibits non-tumorigenic characteristics when used *in vivo* or *in vitro.* MCF10A is typically used as a control cell line to monitor the effects of testing conditions compared to invasive or metastatic cell lines. A study by Qu et al. states that MCF10A is classified as a non-transformed human mammary breast epithelial cell line, but examined a series of markers like luminal, myoepithelial, and stem-like cells in MCF10A cells in 2D and 3D culture, which argues whether MCF10A is a representative model for normal mammary cells[91]. MCF10A is still being used as a suitable model of normal mammary cells, but further investigation is needed.

Extracellular Vesicles

Extracellular vesicles are lipid-bound vesicles that are secreted by cells into the extracellular niche to maintain homeostasis and participate in cell-cell communication. There are two main subtypes of extracellular vesicles: microvesicles and exosomes, which vary in size and release pathways[92]. Microvesicles are particles that range from 100 nm up to 1 μm in diameter and are formed by outward pinching of the cell's plasma[93]. Exosomes are smaller, with sizes ranging from 30 to 150 nm, and are produced by inward pitching of a limited membrane[92,94]. Extracellular vesicles facilitate intracellular communication by transporting proteins, metabolites, nucleic acids, and other biological information to distant locations within the body[95]. In terms of cancer development, extracellular vesicles have been used to demonstrate a strong link between glucose homeostasis and breast cancer proliferation[96]. Additionally, breast cancer cells have been shown to deviate from trajectories during distant migration aided by extracellular vesicles and hyaluronic acid, a glycosaminoglycan, to pre-established metastatic niches[96]. Furthermore, tumor-derived extracellular vesicles have shown to reduce cell adhesion by expressing CD44, a cell surface glycoprotein, which disrupts actin structure and induces tumor spread and metastasis[96].

Breast Metastasis

When identifying stages of breast cancer, the TNM staging system is often used to report severity[97,98]. T refers to the size of the primary tumor, N refers to the number of nearby lymph nodes affects, and M refers to the metastasis status[99]. Of the four stages of breast cancer, metastasis occurs in the last stage (stage IV), where it would be assigned an M index of M1. Approximately 20-30% of patients are diagnosed with metastatic breast cancer, which, to date, remains incurable. 5-year survival rates range from 86-99% for regional and localized breast cancers, respectively[100,101]. Once breast cancer metastasizes, the 5-year survival rate drops as low as 32%[102] (Figure 9).

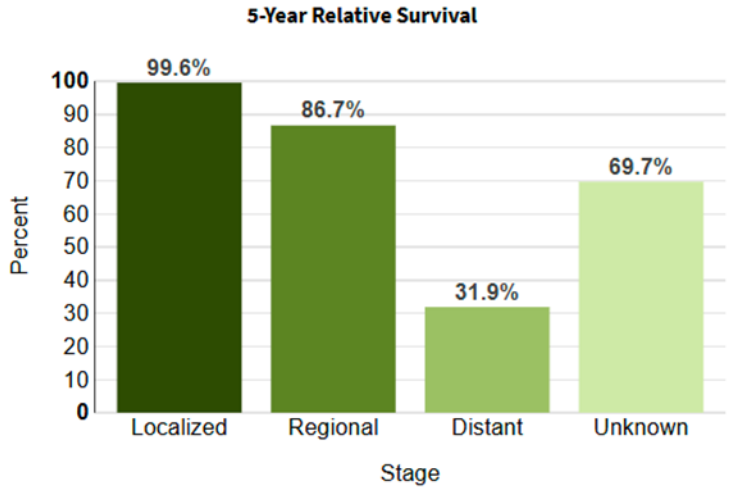

Figure 9. 5-year survival rate of breast cancer at different metastasis locations (adapted from [102])

Bone is the primary location for distant breast metastasis. 70% of patients diagnosed with metastatic breast cancer have bone metastases, and 13.6% of patients diagnosed with stage I to III cancer develop bone metastasis within 15 years[2]. To metastasize to distant sites like the bone, invasive breast carcinoma cells undergo epithelial-to-mesenchymal transition (EMT) and intravasate into lymph nodes or blood vessels[2]. In the systemic circulation system, tumor cells survive due to a variety of stress factors such as chronic immobilization stress, RANKL signaling, and adrenergic stimulus. They then drive extravasation, or mesenchymal-to-epithelial transition (MET), into the bone microenvironment[103]. Once breast cancer is present in the bone niche,

parathyroid hormone-related peptide (PTHrP) is released, which causes a decrease in osteoprotegerin (OPG), a protein that decreases osteoclast activity. This leads to osteolysis and, ultimately, destruction of bone integrity[2]. Once breast cancer metastasizes to the bone microenvironment, the 5-year survival rate drops to 24%[101].

Mechanical Influence of Breast Cancer

With breast cancer having a high likelihood of metastasizing to bone, disease states like osteolytic and osteoblastic lesions could occur, where bone mechanical properties are affected due to the metastatic tumor deregulating bone homeostasis[104]. Osteolytic metastasis is a bone disease state where breast cancer tumor cells accelerate bone loss, preventing new bone growth due to the inhibition of osteoblasts, and the upregulation of bone resorption, osteoclasts[105,106]. On the other hand, osteoblastic metastasis is a disease state where breast cancer cells suppress osteoclast resorption and increase osteoblast formation, causing woven and mechanical changes[104,107,108]. In most cases, breast cancer causes osteolytic conditions (80%), but it has a 20% chance of becoming osteoblastic. The cancer types that we plan on observing, as previously mentioned, are MDA-MB-231 and 468, which are predominantly osteolytic, and T47D, which has shown osteoblastic activity[109,110]. A study conducted by Bianchi et. al looked at the mechanical behavior of osteolytic and osteoblastic bone lesions using a CT-based FE model and found that osteolytic lesions are more likely susceptible to local weakening and deformation[111]. Opposite to that, their FE revealed that osteoblastic lesions are likely to induce stiffening and deformity similar to or lower than non-metastatic cases[111]. As such, the introduction of EVs or BC cells from those associated with osteolytic and osteoblastic lineages are expected to antithetically modify *in vitro* model mechanics.

2.4 Breast-to-Bone Metastasis Models

Using 2D co-culture models to understand the mechanisms of metastasis and the effects of treatments is the current standard for both preclinical and clinical trials. However, 2D co-culture and *in vivo* validation models do not provide enough valuable information to accurately predict drug efficacy or to accurately analyze the spatial architecture of the bone microenvironment[112]. Furthermore, 2D cultures do not allow for communication between tumor and endogenous stromal cells and are unable to replicate the bone remodeling process, which are important when trying to identify the mechanism of aggression in breast-to-bone metastasis[112,113]. Animal models such as rodents are commonly used to validate the efficacy of a therapeutic, but they cannot accurately replicate human physiology. The immune system of rodents and humans are drastically different with regard to disease progression, metabolic reaction, and spontaneity of bone metastasis[114]. An advancement beyond the standard mode would be a bone-on-a-chip or a bioreactor which would enable cross-communication between tumor and endogenous cells but would still fall short in fully replicating and accurately assessing the complexity of the bone microenvironment[113].

3D *in vitro* models are a great alternative for bone modeling due to their ability to mimic the bone microenvironment via structure and formation of extracellular matrix. This allows for a cohesive co-culture environment and for mechanical loading analysis in bone remodeling[115–117]. A study by Jasuja et al. assessed patient-specific metastasis using *in vitro* models using a 10% *in situ HAPclay* with PCL dissolved in 1,4-dioxane and freeze-dried to create a porous 12 x 3 mm (diameter, height) cylinder[118]. This study successfully created a 3D *in vitro* bone niche where hMSCs differentiated into osteoblasts, leading to collagen formation and mineral deposition. Within the co-culture system, NT013 (ER+/PR+) and NT023 (TNBC) cells underwent MET and pathogenic pathways to form tumors on the scaffolds[118]. Furthermore, cytokines were released and

influenced growth within the system, successfully developing a 3D breast cancer bone metastatic model[118]. However, this study conducted a preliminary study using two patients to represent two types of cancer, which provides a strong metastatic *in vitro* model but does not encapsulate other possible variations, such as T47D or MDA-MB-468 patient-like cells. Therefore, future studies need to look into having biological replicates from different patients to fully have a patient-specific *in vitro* model. Despite years of ongoing research, creating a standardized *in vitro* model for breast-to-bone metastasis remains a significant challenge.

2.5 References

1. Breast cancer statistics. World Cancer Research Fund. Accessed April 30, 2025. https://www.wcrf.org/preventing-cancer/cancer-statistics/breast-cancer-statistics/

2. Pulido C, Vendrell I, Ferreira AR, Casimiro S, Mansinho A, Alho I, Costa L. Bone metastasis risk factors in breast cancer. *ecancermedicalscience*. 2017;11:715. doi:10.3332/ecancer.2017.715

3. Taverna S, Giusti I, D'Ascenzo S, Pizzorno L, Dolo V. Breast Cancer Derived Extracellular Vesicles in Bone Metastasis Induction and Their Clinical Implications as Biomarkers. *Int J Mol Sci*. 2020;21(10):3573. doi:10.3390/ijms21103573

4. Forder A, Hsing CY, Trejo Vazquez J, Garnis C. Emerging Role of Extracellular Vesicles and Cellular Communication in Metastasis. *Cells*. 2021;10(12):3429. doi:10.3390/cells10123429

5. Becker A, Thakur BK, Weiss JM, Kim HS, Peinado H, Lyden D. Extracellular vesicles in cancer: cell-to-cell mediators of metastasis. *Cancer Cell*. 2016;30(6):836-848. doi:10.1016/j.ccell.2016.10.009

6. Sakamoto Y, Ochiya T, Yoshioka Y. Extracellular vesicles in the breast cancer brain metastasis: physiological functions and clinical applications. *Front Hum Neurosci*. 2023;17. doi:10.3389/fnhum.2023.1278501

7. Brena D, Huang MB, Bond V. Extracellular vesicle-mediated transport: Reprogramming a tumor microenvironment conducive with breast cancer progression and metastasis. *Transl Oncol*. 2022;15(1):101286. doi:10.1016/j.tranon.2021.101286

8. Giannandrea D, Citro V, Lesma E, Bignotto M, Platonova N, Chiaramonte R. Restoring Tissue Homeostasis at Metastatic Sites: A Focus on Extracellular Vesicles in Bone Metastasis. *Front Oncol*. 2021;11. doi:10.3389/fonc.2021.644109

9. Hart NH, Nimphius S, Rantalainen T, Ireland A, Siafarikas A, Newton RU. Mechanical basis of bone strength: influence of bone material, bone structure and muscle action. *J Musculoskelet Neuronal Interact*. 2017;17(3):114-139.

10. Swaroop Yadav P, Yang Y. Lineage Determination of Osteoblasts and Chondrocytes. In: Zaidi M, ed. *Encyclopedia of Bone Biology*. Academic Press; 2020:397-408. doi:10.1016/B978-0-12-801238-3.11173-0

11. General (US) O of the S. The Basics of Bone in Health and Disease. In: *Bone Health and Osteoporosis: A Report of the Surgeon General*. Office of the Surgeon General (US); 2004. Accessed April 3, 2025. https://www.ncbi.nlm.nih.gov/books/NBK45504/

12. Du Y, Zhang L, Wang Z, Zhao X, Zou J. Endocrine Regulation of Extra-skeletal Organs by Bone-derived Secreted Protein and the effect of Mechanical Stimulation. *Front Cell Dev Biol*. 2021;9. doi:10.3389/fcell.2021.778015

13. Ono N, Kronenberg HM. Chapter 1 - Developmental Biology of Musculoskeletal Tissues for Tissue Engineers. In: Stoddart MJ, Craft AM, Pattappa G, Gardner OFW, eds. *Developmental Biology and Musculoskeletal Tissue Engineering*. Academic Press; 2018:1-24. doi:10.1016/B978-0-12-811467-4.00001-2

14. World D. Human Body Facts: Huge List of Amazing Trivia | DW. June 11, 2015. Accessed April 3, 2025. https://www.disabled-world.com/medical/human-body-facts.php

15. Xue N, Ding X, Huang R, Jiang R, Huang H, Pan X, Min W, Chen J, Duan JA, Liu P, Wang Y. Bone Tissue Engineering in the Treatment of Bone Defects. *Pharmaceuticals*. 2022;15(7):879. doi:10.3390/ph15070879

16. Bone Cortical And Cancellous. Physiopedia. Accessed April 3, 2025. https://www.physiopedia.com/Bone_Cortical_And_Cancellous

17. Morgan EF, Unnikrisnan GU, Hussein AI. Bone Mechanical Properties in Healthy and Diseased States. *Annu Rev Biomed Eng*. 2018;20:119-143. doi:10.1146/annurev-bioeng-062117-121139

18. 7.4: Structure of Bone. Biology LibreTexts. August 16, 2021. Accessed April 3, 2025. https://bio.libretexts.org/Courses/Minnesota_State_Community_and_Technical_College/Biology_of_Human_Concerns_(Daniels)/07%3A_Skeletal_System/7.04%3A_Structure_of_Bone

19. Periosteum. Physiopedia. Accessed April 3, 2025. https://www.physiopedia.com/Periosteum

20. Buckwalter JA, Cooper RR. Bone structure and function. *Instr Course Lect*. 1987;36:27-48.

21. Nahian A, Chauhan PR. Histology, Periosteum And Endosteum. In: *StatPearls*. StatPearls Publishing; 2025. Accessed April 3, 2025. http://www.ncbi.nlm.nih.gov/books/NBK557584/

22. Dwek JR. The periosteum: what is it, where is it, and what mimics it in its absence? *Skeletal Radiol*. 2010;39(4):319-323. doi:10.1007/s00256-009-0849-9

23. Chang B, Liu X. Osteon: Structure, Turnover, and Regeneration. *Tissue Eng Part B Rev*. 2022;28(2):261-278. doi:10.1089/ten.teb.2020.0322

24. Chang B, Liu X. Osteon: Structure, Turnover, and Regeneration. *Tissue Eng Part B Rev*. 2022;28(2):261-278. doi:10.1089/ten.teb.2020.0322

25. Collins CJ, Andriotis OG, Nedelkovski V, Frank M, Katsamenis OL, Thurner PJ. Bone Micro- and Nanomechanics. In: Narayan R, ed. *Encyclopedia of Biomedical Engineering*. Elsevier; 2019:22-44. doi:10.1016/B978-0-12-801238-3.99937-9

26. Clarke B. Normal Bone Anatomy and Physiology. *Clin J Am Soc Nephrol CJASN*. 2008;3(Suppl 3):S131-S139. doi:10.2215/CJN.04151206

27. Park Y, Cheong E, Kwak JG, Carpenter R, Shim JH, Lee J. Trabecular bone organoid model for studying the regulation of localized bone remodeling. *Sci Adv*. 2021;7(4):eabd6495. doi:10.1126/sciadv.abd6495

28. Hart NH, Nimphius S, Rantalainen T, Ireland A, Siafarikas A, Newton RU. Mechanical basis of bone strength: influence of bone material, bone structure and muscle action. *J Musculoskelet Neuronal Interact*. 2017;17(3):114-139.

29. Walsh JS. Normal bone physiology, remodelling and its hormonal regulation. *Surg Oxf*. 2015;33(1):1-6. doi:10.1016/j.mpsur.2014.10.010

30. Oftadeh R, Perez-Viloria M, Villa-Camacho JC, Vaziri A, Nazarian A. Biomechanics and Mechanobiology of Trabecular Bone: A Review. *J Biomech Eng*. 2015;137(010802). doi:10.1115/1.4029176

31. Goda I, Ganghoffer JF. A thermodynamic-based principle for accretion phenomena applied to the modeling of bone external remodeling. *Arch Appl Mech*. 2022;92(4):1367-1380. doi:10.1007/s00419-022-02114-4

32. Burr DB, Akkus O. Chapter 1 - Bone Morphology and Organization. In: Burr DB, Allen MR, eds. *Basic and Applied Bone Biology*. Academic Press; 2014:3-25. doi:10.1016/B978-0-12-416015-6.00001-0

33. Tripathy N, Perumal E, Ahmad R, Song JE, Khang G. Chapter 40 - Hybrid Composite Biomaterials. In: Atala A, Lanza R, Mikos AG, Nerem R, eds. *Principles of Regenerative Medicine (Third Edition)*. Academic Press; 2019:695-714. doi:10.1016/B978-0-12-809880-6.00040-0

34. role of cortical bone and its microstructure in bone strength | Age and Ageing | Oxford Academic. Accessed April 4, 2025. https://academic.oup.com/ageing/article/35/suppl_2/ii27/15730?login=true

35. Šromová V, Sobola D, Kaspar P. A Brief Review of Bone Cell Function and Importance. *Cells*. 2023;12(21):2576. doi:10.3390/cells12212576

36. Feng X. Chemical and Biochemical Basis of Cell-Bone Matrix Interaction in Health and Disease. *Curr Chem Biol*. 2009;3(2):189-196. doi:10.2174/187231309788166398

37. Boyce BF, Xing L. The RANKL/RANK/OPG pathway. *Curr Osteoporos Rep*. 2007;5(3):98-104. doi:10.1007/s11914-007-0024-y

38. Caetano-Lopes J, Canhão H, Eurico Fonseca J. OSTEOBLASTS AND BONE FORMATION. *Acta Reumatol Port*. 2007;32(2):103-110.

39. Aarden EM, Nijweide PJ, Burger EH. Function of osteocytes in bone. *J Cell Biochem*. 1994;55(3):287-299. doi:10.1002/jcb.240550304

40. Florencio-Silva R, Sasso GR da S, Sasso-Cerri E, Simões MJ, Cerri PS. Biology of Bone Tissue: Structure, Function, and Factors That Influence Bone Cells. *BioMed Res Int*. 2015;2015:421746. doi:10.1155/2015/421746

41. Schaffler MB, Kennedy OD. Osteocyte Signaling in Bone. *Curr Osteoporos Rep*. 2012;10(2):118-125. doi:10.1007/s11914-012-0105-4

42. Osteocyte: the unrecognized side of bone tissue | Osteoporosis International. Accessed April 7, 2025. https://link.springer.com/article/10.1007/s00198-010-1194-5

43. Nahian A, AlEssa AM. Histology, Osteocytes. In: *StatPearls*. StatPearls Publishing; 2025. Accessed April 7, 2025. http://www.ncbi.nlm.nih.gov/books/NBK558990/

44. Choi JUA, Kijas AW, Lauko J, Rowan AE. The Mechanosensory Role of Osteocytes and Implications for Bone Health and Disease States. *Front Cell Dev Biol*. 2022;9. doi:10.3389/fcell.2021.770143

45. Aharoni S, Rittel D, Shemtov-Yona K. Factual observations of dynamic bone crushing. *Sci Rep*. 2024;14(1):25597. doi:10.1038/s41598-024-77717-8

46. Nordin M, Frankel VH. *Basic Biomechanics of the Musculoskeletal System*. Lippincott Williams & Wilkins; 2001.

47. Oftadeh R, Perez-Viloria M, Villa-Camacho JC, Vaziri A, Nazarian A. Biomechanics and Mechanobiology of Trabecular Bone: A Review. *J Biomech Eng*. 2015;137(1):0108021-01080215. doi:10.1115/1.4029176

48. Choi S, Hunt E, Shangin EA, Bahranifard Z, Nguyen E, Collins CJ, Whittington AR. Dynamic Micromechanical Characterization of 3D Printed Bone In Vitro Models Manufactured via Vat Photopolymerization. *Adv Funct Mater*. n/a(n/a):2418547. doi:10.1002/adfm.202418547

49. Animal Models for Evaluation of Bone Implants and Devices - L. M. Wancket, 2015. Accessed April 13, 2025. https://journals.sagepub.com/doi/10.1177/0300985815593124

50. Stein M, Elefteriou F, Busse B, Fiedler IAK, Kwon RY, Farell E, Ahmad M, Ignatius A, Grover L, Geris L, Tuckermann J. Why animal experiments are still indispensable in bone research: A statement by the European Calcified Tissue Society. *J Bone Miner Res Off J Am Soc Bone Miner Res*. 2023;38(8):1045-1061. doi:10.1002/jbmr.4868

51. Wei J, Chen X, Xu Y, Shi L, Zhang M, Nie M, Liu X. Significance and considerations of establishing standardized critical values for critical size defects in animal models of bone tissue regeneration. *Heliyon*. 2024;10(13):e33768. doi:10.1016/j.heliyon.2024.e33768

52. Wancket LM. Animal Models for Evaluation of Bone Implants and Devices: Comparative Bone Structure and Common Model Uses. *Vet Pathol*. 2015;52(5):842-850. doi:10.1177/0300985815593124

53. Wei J, Chen X, Xu Y, Shi L, Zhang M, Nie M, Liu X. Significance and considerations of establishing standardized critical values for critical size defects in animal models of bone tissue regeneration. *Heliyon*. 2024;10(13):e33768. doi:10.1016/j.heliyon.2024.e33768

54. Bonucci E, Ballanti P. Osteoporosis—Bone Remodeling and Animal Models. *Toxicol Pathol*. 2014;42(6):957-969. doi:10.1177/0192623313512428

55. Yuste I, Luciano FC, González-Burgos E, Lalatsa A, Serrano DR. Mimicking bone microenvironment : 2D and 3D in vitro models of human osteoblasts. *Pharmacol Res*. 2021;169. Accessed April 16, 2025. https://doi.org/10.1016/j.phrs.2021.105626

56. Duval K, Grover H, Han LH, Mou Y, Pegoraro AF, Fredberg J, Chen Z. Modeling Physiological Events in 2D vs. 3D Cell Culture. *Physiology*. 2017;32(4):266-277. doi:10.1152/physiol.00036.2016

57. Substrate topography shapes cell function - Soft Matter (RSC Publishing). Accessed April 16, 2025. https://pubs.rsc.org/en/content/articlelanding/2009/sm/b910132m

58. Ball M, Grant DM, Lo WJ, Scotchford CA. The effect of different surface morphology and roughness on osteoblast-like cells. *J Biomed Mater Res A*. 2008;86A(3):637-647. doi:10.1002/jbm.a.31652

59. Lamouline A, Bersini S, Moretti M. In vitro models of breast cancer bone metastasis: analyzing drug resistance through the lens of the microenvironment. *Front Oncol*. 2023;13:1135401. doi:10.3389/fonc.2023.1135401

60. Modulation of In Vitro Angiogenesis in a Three-Dimensional Spheroidal Coculture Model for Bone Tissue Engineering | Tissue Engineering. Accessed April 16, 2025. https://www.liebertpub.com/doi/10.1089/ten.2004.10.1536?url_ver=Z39.88-2003&rfr_id=ori%3Arid%3Acrossref.org&rfr_dat=cr_pub++0pubmed

61. Vinatier C, Magne D, Weiss P, Trojani C, Rochet N, Carle GF, Vignes-Colombeix C, Chadjichristos C, Galera P, Daculsi G, Guicheux J. A silanized hydroxypropyl methylcellulose hydrogel for the three-dimensional culture of chondrocytes. *Biomaterials*. 2005;26(33):6643-6651. doi:10.1016/j.biomaterials.2005.04.057

62. Parsons AJ, Ahmed I, Han N, Felfel R, Rudd CD. Mimicking Bone Structure and Function with Structural Composite Materials. *J Bionic Eng*. 2010;7:S1-S10. doi:10.1016/S1672-6529(09)60211-0

63. Lee SS, Du X, Kim I, Ferguson SJ. Scaffolds for bone-tissue engineering. *Matter*. 2022;5(9):2722-2759. doi:10.1016/j.matt.2022.06.003

64. Percival KM, Paul V, Husseini GA. Recent Advancements in Bone Tissue Engineering: Integrating Smart Scaffold Technologies and Bio-Responsive Systems for Enhanced Regeneration. *Int J Mol Sci*. 2024;25(11):6012. doi:10.3390/ijms25116012

65. Olevsky LM, Anup A, Jacques M, Keokominh N, Holmgren EP, Hixon KR. Direct Integration of 3D Printing and Cryogel Scaffolds for Bone Tissue Engineering. *Bioengineering*. 2023;10(8):889. doi:10.3390/bioengineering10080889

66. de Leeuw AM, Graf R, Lim PJ, Zhang J, Schädli GN, Peterhans S, Rohrbach M, Giunta C, Rüger M, Rubert M, Müller R. Physiological cell bioprinting density in human bone-derived cell-laden scaffolds enhances matrix mineralization rate and stiffness under dynamic loading. *Front Bioeng Biotechnol*. 2024;12:1310289. doi:10.3389/fbioe.2024.1310289

67. Teixeira AM, Martins P. A review of bioengineering techniques applied to breast tissue: Mechanical properties, tissue engineering and finite element analysis. *Front Bioeng Biotechnol*. 2023;11. doi:10.3389/fbioe.2023.1161815

68. CDC. Breast Cancer Basics. Breast Cancer. February 3, 2025. Accessed April 7, 2025. https://www.cdc.gov/breast-cancer/about/index.html

69. Sung H, Ferlay J, Siegel RL, Laversanne M, Soerjomataram I, Jemal A, Bray F. Global Cancer Statistics 2020: GLOBOCAN Estimates of Incidence and Mortality Worldwide for 36 Cancers in 185 Countries. *CA Cancer J Clin*. 2021;71(3):209-249. doi:10.3322/caac.21660

70. Xiong X, Zheng LW, Ding Y, Chen YF, Cai YW, Wang LP, Huang L, Liu CC, Shao ZM, Yu KD. Breast cancer: pathogenesis and treatments. *Signal Transduct Target Ther*. 2025;10(1):1-33. doi:10.1038/s41392-024-02108-4

71. Łukasiewicz S, Czeczelewski M, Forma A, Baj J, Sitarz R, Stanisławek A. Breast Cancer—Epidemiology, Risk Factors, Classification, Prognostic Markers, and Current Treatment Strategies—An Updated Review. *Cancers*. 2021;13(17):4287. doi:10.3390/cancers13174287

72. Giaquinto AN, Sung H, Miller KD, Kramer JL, Newman LA, Minihan A, Jemal A, Siegel RL. Breast Cancer Statistics, 2022. *CA Cancer J Clin*. 2022;72(6):524-541. doi:10.3322/caac.21754

73. Menon G, Alkabban FM, Ferguson T. Breast Cancer. In: *StatPearls*. StatPearls Publishing; 2025. Accessed April 7, 2025. http://www.ncbi.nlm.nih.gov/books/NBK482286/

74. Types of Breast Cancer. Accessed April 7, 2025. https://www.breastcancer.org/types

75. Types of Breast Cancer | About Breast Cancer. Accessed April 7, 2025. https://www.cancer.org/cancer/types/breast-cancer/about/types-of-breast-cancer.html

76. Kirkby M, Popatia AM, Lavoie JR, Wang L. The Potential of Hormonal Therapies for Treatment of Triple-Negative Breast Cancer. *Cancers*. 2023;15(19):4702. doi:10.3390/cancers15194702

77. Welsh J. Chapter 40 - Animal Models for Studying Prevention and Treatment of Breast Cancer. In: Conn PM, ed. *Animal Models for the Study of Human Disease*. Academic Press; 2013:997-1018. doi:10.1016/B978-0-12-415894-8.00040-3

78. Huang Z, Yu P, Tang J. Characterization of Triple-Negative Breast Cancer MDA-MB-231 Cell Spheroid Model . *OncoTargets Ther*. 2020;13:5395-5405. doi:10.2147/OTT.S249756

79. Tate CR, Rhodes LV, Segar HC, Driver JL, Pounder FN, Burow ME, Collins-Burow BM. Targeting triple-negative breast cancer cells with the histone deacetylase inhibitor panobinostat. *Breast Cancer Res*. 2012;14(3):R79. doi:10.1186/bcr3192

80. MDA-MB-231 - HTB-26 | ATCC. Accessed April 8, 2025. https://www.atcc.org/products/htb-26

81. Franchi M, Piperigkou Z, Karamanos KA, Franchi L, Masola V. Extracellular Matrix-Mediated Breast Cancer Cells Morphological Alterations, Invasiveness, and Microvesicles/Exosomes Release. *Cells*. 2020;9(9):2031. doi:10.3390/cells9092031

82. MDA-MB-468 - HTB-132 | ATCC. Accessed April 8, 2025. https://www.atcc.org/products/htb-132

83. G6PD (Glucose-6-Phosphate Dehydrogenase) Deficiency. April 16, 2024. Accessed April 8, 2025. https://www.hopkinsmedicine.org/health/conditions-and-diseases/g6pd-glucose6phosphate-dehydrogenase-deficiency

84. Hemolytic anemia: Symptoms, diagnosis, and treatment. August 31, 2022. Accessed April 29, 2025. https://www.medicalnewstoday.com/articles/hemolytic-anemia

85. Grace RF, Glenthoej A, Barcellini W, Verhovsek M, Rothman JA, Morado M, Layton DM, Andres O, Galactéros F, Van Beers EJ, Onodera K, Viprakasit V, Chonat S, Porter JB, Judge MP, Kosinski PA, Hawkins P, Gheuens S, Xu E, McGee B, Beynon V, Al-Samkari H. Durability of Hemoglobin Response and Reduction in Transfusion Burden Is Maintained over Time in Patients with Pyruvate Kinase Deficiency Treated with Mitapivat in a Long-Term Extension Study. *Blood*. 2021;138(Supplement 1):848-848. doi:10.1182/blood-2021-147711

86. Audia S, Bach B, Samson M, Lakomy D, Bour JB, Burlet B, Guy J, Duvillard L, Branger M, Leguy-Seguin V, Berthier S, Michel M, Bonnotte B. Venous thromboembolic events during warm autoimmune hemolytic anemia. Garcia De Frutos P, ed. *PLOS ONE*. 2018;13(11):e0207218. doi:10.1371/journal.pone.0207218

87. Yu S, Kim T, Yoo KH, Kang K. The T47D cell line is an ideal experimental model to elucidate the progesterone-specific effects of a luminal A subtype of breast cancer. *Biochem Biophys Res Commun*. 2017;486(3):752-758. doi:10.1016/j.bbrc.2017.03.114

88. Holen I, Walker M, Nutter F, Fowles A, Evans CA, Eaton CL, Ottewell PD. Oestrogen receptor positive breast cancer metastasis to bone: inhibition by targeting the bone

microenvironment in vivo. *Clin Exp Metastasis*. 2016;33(3):211-224. doi:10.1007/s10585-015-9770-x

89. Montt-Guevara MM, Shortrede JE, Giretti MS, Giannini A, Mannella P, Russo E, Genazzani AD, Simoncini T. Androgens Regulate T47D Cells Motility and Invasion through Actin Cytoskeleton Remodeling. *Front Endocrinol*. 2016;7:136. doi:10.3389/fendo.2016.00136

90. MCF cell lines that transformed breast cancer research. Accessed April 9, 2025. https://www.karmanos.org/karmanos/mcf-cell-lines

91. Qu Y, Han B, Yu Y, Yao W, Bose S, Karlan BY, Giuliano AE, Cui X. Evaluation of MCF10A as a Reliable Model for Normal Human Mammary Epithelial Cells. *PLoS ONE*. 2015;10(7):e0131285. doi:10.1371/journal.pone.0131285

92. Doyle LM, Wang MZ. Overview of Extracellular Vesicles, Their Origin, Composition, Purpose, and Methods for Exosome Isolation and Analysis. *Cells*. 2019;8(7):727. doi:10.3390/cells8070727

93. Zaborowski MP, Balaj L, Breakefield XO, Lai CP. Extracellular Vesicles: Composition, Biological Relevance, and Methods of Study. *Bioscience*. 2015;65(8):783-797. doi:10.1093/biosci/biv084

94. Dai YD, Dias P. Exosomes or Microvesicles, a Secreted Subcellular Organelle Contributing to Inflammation and Diabetes. *Diabetes*. 2018;67(11):2154-2156. doi:10.2337/dbi18-0021

95. Zhang X, Liu D, Gao Y, Lin C, An Q, Feng Y, Liu Y, Liu D, Luo H, Wang D. The Biology and Function of Extracellular Vesicles in Cancer Development. *Front Cell Dev Biol*. 2021;9. doi:10.3389/fcell.2021.777441

96. Zhang X, Wang C, Yu J, Bu J, Ai F, Wang Y, Lin J, Zhu X. Extracellular vesicles in the treatment and diagnosis of breast cancer: a status update. *Front Endocrinol*. 2023;14:1202493. doi:10.3389/fendo.2023.1202493

97. Association AL. State of Lung Cancer | Key Findings. Accessed April 9, 2025. https://www.lung.org/research/state-of-lung-cancer/key-findings

98. Menon G, Alkabban FM, Ferguson T. Breast Cancer. In: *StatPearls*. StatPearls Publishing; 2025. Accessed April 9, 2025. http://www.ncbi.nlm.nih.gov/books/NBK482286/

99. Cancer Staging - NCI. March 9, 2015. Accessed April 9, 2025. https://www.cancer.gov/about-cancer/diagnosis-staging/staging

100. Breast Cancer Survival Rate. moffitt. Accessed April 9, 2025. https://www.moffitt.org/cancers/breast-cancer/survival-rate/

101. Iii WJ, Krishnan V, Mastro AM. The Breast Cancer Metastases in Bone Conundrum. In: *Madame Curie Bioscience Database [Internet]*. Landes Bioscience; 2013. Accessed April 9, 2025. https://www.ncbi.nlm.nih.gov/books/NBK169226/

102. Cancer of the Breast (Female) - Cancer Stat Facts. SEER. Accessed April 9, 2025. https://seer.cancer.gov/statfacts/html/breast.html

103. Conceição F, Sousa DM, Paredes J, Lamghari M. Sympathetic activity in breast cancer and metastasis: partners in crime. *Bone Res*. 2021;9:9. doi:10.1038/s41413-021-00137-1

104. Sarazin BA, Ihle CL, Owens P, Lynch ME. Mechanobiology of Bone Metastatic Cancer. *Curr Osteoporos Rep*. 2021;19(6):580-591. doi:10.1007/s11914-021-00704-9

105. Venetis K, Piciotti R, Sajjadi E, Invernizzi M, Morganti S, Criscitiello C, Fusco N. Breast Cancer with Bone Metastasis: Molecular Insights and Clinical Management. *Cells*. 2021;10(6):1377. doi:10.3390/cells10061377

106. Kolb AD, Shupp AB, Mukhopadhyay D, Marini FC, Bussard KM. Osteoblasts are "educated" by crosstalk with metastatic breast cancer cells in the bone tumor microenvironment. *Breast Cancer Res BCR*. 2019;21:31. doi:10.1186/s13058-019-1117-0

107. Clines KL, Clines GA. DKK1 and Kremen Expression Predicts the Osteoblastic Response to Bone Metastasis. *Transl Oncol*. 2018;11(4):873-882. doi:10.1016/j.tranon.2018.04.013

108. Yin JJ, Mohammad KS, Käkönen SM, Harris S, Wu-Wong JR, Wessale JL, Padley RJ, Garrett IR, Chirgwin JM, Guise TA. A causal role for endothelin-1 in the pathogenesis of osteoblastic bone metastases. *Proc Natl Acad Sci*. 2003;100(19):10954-10959. doi:10.1073/pnas.1830978100

109. Guise TA, Yin JJ, Mohammad KS. Role of endothelin-1 in osteoblastic bone metastases. *Cancer*. 2003;97(S3):779-784. doi:10.1002/cncr.11129

110. Clines KL, Clines GA. DKK1 and Kremen Expression Predicts the Osteoblastic Response to Bone Metastasis. *Transl Oncol*. 2018;11(4):873-882. doi:10.1016/j.tranon.2018.04.013

111. Bianchi D, Falcinelli C, Molinari L, Gizzi A, Di Martino A. Osteolytic vs. Osteoblastic Metastatic Lesion: Computational Modeling of the Mechanical Behavior in the Human Vertebra after Screws Fixation Procedure. *J Clin Med*. 2022;11(10):2850. doi:10.3390/jcm11102850

112. Lamouline A, Bersini S, Moretti M. In vitro models of breast cancer bone metastasis: analyzing drug resistance through the lens of the microenvironment. *Front Oncol*. 2023;13. doi:10.3389/fonc.2023.1135401

113. Hughes AM, Kolb AD, Shupp AB, Shine KM, Bussard KM. Printing the Pathway Forward in Bone Metastatic Cancer Research: Applications of 3D Engineered Models and Bioprinted Scaffolds to Recapitulate the Bone–Tumor Niche. *Cancers*. 2021;13(3):507. doi:10.3390/cancers13030507

114. Yu Y, Li K, Peng Y, Wu W, Chen F, Shao Z, Zhang Z. Animal models of cancer metastasis to the bone. *Front Oncol*. 2023;13:1165380. doi:10.3389/fonc.2023.1165380

115. Kumar V, Naqvi SM, Verbruggen A, McEvoy E, McNamara LM. A mechanobiological model of bone metastasis reveals that mechanical stimulation inhibits the pro-osteolytic effects of breast cancer cells. *Cell Rep*. 2024;43(5):114043. doi:10.1016/j.celrep.2024.114043

116. Bray LJ, Secker C, Murekatete B, Sievers J, Binner M, Welzel PB, Werner C. Three-Dimensional In Vitro Hydro- and Cryogel-Based Cell-Culture Models for the Study of Breast-Cancer Metastasis to Bone. *Cancers*. 2018;10(9):292. doi:10.3390/cancers10090292

117. Laranga R, Duchi S, Ibrahim T, Guerrieri AN, Donati DM, Lucarelli E. Trends in Bone Metastasis Modeling. *Cancers*. 2020;12(8):2315. doi:10.3390/cancers12082315

118. Jasuja H, Solaymani Mohammadi F, Kim J, Gaba A, Katti DR, Katti KS. Patient-Derived Breast Cancer Bone Metastasis In Vitro Model Using Bone-Mimetic Nanoclay Scaffolds. *J Tissue Eng Regen Med*. 2023;2023(1):5753666. doi:10.1155/2023/5753666

120. Unexpected Preferential Brain Metastases with a Human Breast Tumor Cell Line MDA-MB-231 in BALB/c Nude Mice - A. A. El-Mabhouh, P. N. Nation, A. Kaddoura, J. R. Mercer, 2008. Accessed May 21, 2025. https://journals.sagepub.com/doi/10.1354/vp.45-6-941?icid=int.sj-full-text.similar-articles.7

121. Hamester F, Stürken C, Saygi C, Qi M, Legler K, Gorzelanny C, Robador JR, Schmalfeldt B, Laakmann E, Müller V, Witzel I, Oliveira-Ferrer L. Insights into the Steps of Breast Cancer–Brain Metastases Development: Tumor Cell Interactions with the Blood–Brain Barrier. *Int J Mol Sci*. 2022;23(3):1900. doi:10.3390/ijms23031900

3 Specific Aim 1

3.1 Preamble

The following chapter is comprised of sections from a published collaborative journal article, where I contributed as a co-first author[48]. The contributing authors are Edward Shangin, Elizabeth Hunt, Sera Choi, Zahra Bahranifard, Dr. Abby Whittington, and Dr. Caitlyn Collins. For my thesis, I took methods created by Zahra Bahranifard (scaffold printing), Elizabeth Hunt (DMA testing), and Sera Choi (confocal microscopy) and adapted them as part of my thesis. Furthermore, I seeded scaffolds with human osteoblasts (1.19 hFOB, ATCC), as opposed to NIH 3T3 Fibroblasts from our previous study, and conducted longer cell culture out to 21 days post-seeding.

3.2 Introduction

This study's primary objective is to characterize extracellular matrix (ECM) formation and maturation in an *in vitro* bone tissue culture model seeded with human osteoblasts (1.19 hFOB). This will be accomplished using various imaging modalities, including scanning electron microscopy (SEM), microcomputed tomography (μCT), and dynamic mechanical analysis (DMA). The driving hypothesis is that long-term static culture of human osteoblasts, compared to murine fibroblasts, will more accurately mimic the native bone microenvironment, leading to enhanced mineral deposition and improved mechanical properties, as measured through imaging and DMA.

3.3 Methods and Materials

Resin Formulation

Resin comprised of 50 wt.% epoxidized soybean oil acrylate (ESOA, Sigma-Aldrich) and 50 wt.% polyethylene glycol diacrylate (PEGDA, Sigma-Aldrich, MW = 575 g mol-1) was formulated and used to print the scaffold geometries in 3D. Detailed material comprehension can be found in Chartrain et. al[119]. Additional 1 wt.% diphenyl(2,4,6-trimethylbenzoyl) phosphine oxide photoinitiator (TPO, Sigma-Aldrich) and 0.20 wt.% 2,5-bis(5-tert-butyl-benzoxazol-2-yl)

thiophene UV absorber (BBOT, TCI Chemicals) additives were added to promote photopolymerization and UV absorption, which allowed the resin to cure fully.

Scaffolding Fabrication

Two targeted scaffolds, Voronoi and Truncated Octahedron, were designed using nTopology (Figure 1) to mimic the bone microenvironment. Scaffolds were fabricated on an Autodesk Ember, which vat photopolymerizes a specimen from the bottom up. The printer is equipped with a building area of approximately 40 x 64 mm, a maximum height of 134 mm, and a projected pixel size of 50 μm. The light source of the system utilizes a 5W power output and emits a 405 nm wavelength for 2.5 seconds per layer on average. All layers were printed at 0.1 mm until a total height of 10 mm was achieved. After printing, burn-in layers were extracted, and then scaffolds were immersed in 70% isopropyl alcohol for one minute and cured once more for a minute under a 405 nm UV lamp. Additional porosity and strut thickness details are described in Choi et. al.

Seeding and Cell Culture

Prior to osteoblast seeding, all materials were placed in a biosafety cabinet to ensure a sterile environment. The scaffold underwent an additional sterilization involving a 70% ethanol wash for an hour (room temperature). After sterilization, three 30-minute static washes of phosphate-buffered saline (1X PBS, pH 7.4) were performed. Following the PBS washes, a final 30-minute wash of complete osteogenic media supplemented with DMEM F-12 (ATCC), 10% FBS (ATCC), and 3 ml of 20X G-418 (Thermo-Fisher) was carried out to ensure all traces of ethanol were removed.

Scaffolds were seeded with 2.5 x 10^4 human osteoblasts (ATCC 1.19 hFOBs) and left to attach for 30 minutes in the incubator (37°C, 5% CO_2) before adding 1 ml of osteogenic media. Seeded scaffolds were left to culture for 7 (n = 5/geometry), 14 (n = 5/geometry), and 21 (n =

5/geometry) days under static conditions. Unseeded control scaffolds also underwent 7 (n = 1/geometry), 14 (n = 1/geometry), and 21 (n = 1/geometry) days of static culture to establish a baseline response to the osteogenic media. Following each culture time, scaffolds were immersed in 1 ml of 10% buffered formalin for five minutes. The scaffolds were then washed with 1X PBS for two minutes and immersed in another 1 ml of 10% buffered formalin for 20 minutes to fix the cells. After fixation, scaffolds were rinsed with 1X PBS for one minute to remove excess formalin. Once all samples were fixed, seeded (n = 3/geometry/culture time) and unseeded scaffolds (n = 1/geometry/culture time) were used for mechanical testing. Another set of seeded scaffolds (n = 1/geometry/culture time) was kept for SEM and μCT imaging. Then, the last set of seeded scaffolds (n = 1 geometry/culture time) were cut in half with the middle facing up, and stained with SYTOX™ Green (Thermo-Fisher) and Phalloidin–Atto 565 (Sigma-Aldrich) following the manufacturer's protocols, respectively.

Micro-Computed Tomography

The microstructure of the seeded (n = 1/geometry for 7-, 14-, 21-day cultures) scaffolds were analyzed using micro-computed tomography (μCT, Nikon VOXLS 40 C 450). μCT images were captured using a rotating 225 kV source. A target pixel size range of 10 - 15 μm was determined to accurately assess the microstructure. The X-ray tube was operated at 160 kV with a current of 188 μA and 2280 projections. Reconstructions were carried out using Nikon CT Pro 3D, which converted the raw projections into TIFF files. Segmentation and image processing were performed using DragonFly (Comet Technologies). From μCT images, bone volume fraction (BV/TV), total volume, average trabecular separation, and average trabecular thickness measurements were extracted for analysis.

Dynamic Mechanical Analysis

To mechanically characterize the scaffolds, dynamic mechanical analysis (DMA, Electroforce 3200) was performed on the 1.19 hFOBs seeded (n = 3/geometry for 7-, 14-, 21-day cultures) and unseeded (n = 1/geometry for 7-, 14-, 21-day cultures) scaffolds through cyclic compressive loading. A strain sweep was used to analyze how different cell types, culture times, and scaffold microstructures impact the storage modulus (E'), loss modulus (E"), and loss factor (tan δ) of the bone tissue culture model. The strain sweep was conducted at a frequency of 0.1 Hz with an initial strain of 2% and a step size of 1% applied strain until 10% strain was reached. All samples were submerged in phosphate-buffered saline (1x PBS, pH 7.4) at 37 °C (Figure 10) during testing to keep them hydrated.

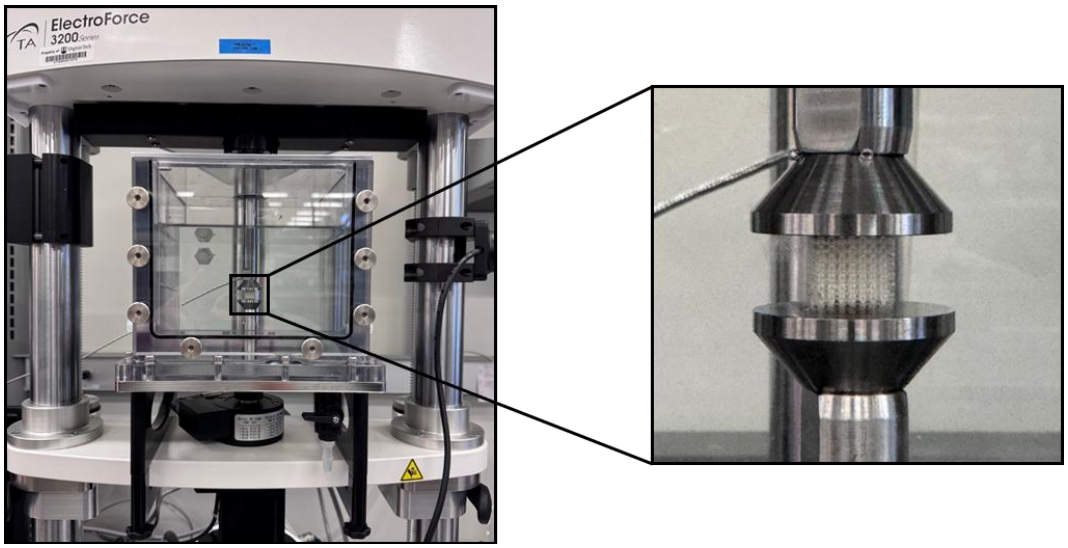

Figure 10. DMA compression testing setup (ElectroForce 3200, TA Instruments) outfitted with a temperature-controlled water bath filled with phosphate-buffered saline (1x PBS, pH 7.4) solution at 37°C and 450N load cell.

Scanning Electron Microscopy

Before scanning electron microscopy (SEM) could be performed on the seeded scaffolds, a critical point drying (CPD) step was required to ensure that successful gold sputter-coating was complete. Seeded scaffolds went through a stepped ethanol dehydration (25%, 50%, 70%, 95%, 100%) process before CPD. This involved submerging the samples in 2 ml of each ethanol concentration for 10 minutes, then transferring them into a critical point dryer (EM CPD300,

Leica). The scaffolds went through a 2-hour drying process, which consisted of cooling, addition of CO_2, gas exchange, heating, and a final release of gas. Scaffolds were then quickly transferred to a 24-well plate (Thermo-Fisher), wrapped in parafilm, and placed into a desiccator to ensure no exposure to moisture occurred.

To prepare each sample for SEM imaging, scaffolds were placed in a sputter-coater (DII-29010SCTR Smart Coater) and coated with gold particles for 1 minute. Samples were then placed in the SEM (JCM-7000, JEOL Ltd.), where surface images were taken at resolutions of 1280 x 1024 pixels and 5180 x 4096 pixels. After surface imaging, each geometry was characterized to observe elements of interest (Mg, Ca, K, and P) after each culture time, respectively. Elemental quantitative maps using SEM Energy Dispersive X-ray (EDX) were produced to analyze element distribution and relationships to regions that had visible cell exposure at each culture time point.

Statistical Analysis

Mechanical data was analyzed using a three-way ANOVA from Python's stats library to identify significant differences between scaffold geometry, culture time, and dynamic mechanical properties. An additional two-way ANOVA post-hoc analysis was performed to establish significance between individual groups ($\alpha = 0.05$). A z-score normalization analysis was also carried out using Microsoft Excel and Python, using a threshold of ±3 standard deviations from the mean to identify any potential outliers in the mechanical testing data. An effective size calculator and power analysis were used to calculate the sample size needed to achieve significance.

3.4 Results

Micro-Computed Tomography

After culturing, seeded scaffolds were examined using μCT and manually segmented to identify porosity, strut thickness, and trabecular separation. Seeded scaffold measurements were

compared to the computer-aided design (CAD) ideal printing parameters (Table 1). Of all the samples, 7-day Voronoi scaffolds achieved the highest percent difference (7.25%) in porosity and the second lowest porosity value (74.4%). For the TO scaffolds, porosity stayed relatively consistent (79%) with the CAD porosity (79.1%) until the 21-day time point, at which point porosity saw a decrease (73.8%). Moving on to strut thickness, Voronoi scaffolds at all culture times had the highest percentage difference and were generally larger than those of TO scaffolds and ideal parameters. However, TO saw a steadier increase in strut thickness over time compared to Voronoi. 7-day Voronoi had the lowest trabecular separation measurement, along with a lower comparative porosity. In Table 1, it is observed that TO geometry typically has the lowest percentage difference and overall, the lower variance in each measurement.

Table 1. Porosity, strut thickness, and trabecular separation data from the nTopology CAD and μCT seeded scaffolds (n = 1/geometry and culture time).

Geometry	CAD	Printed, μCT	Percentage Difference (%)
Porosity (%)			
7-day Voronoi	80	74.4	7.25%
14-day Voronoi		76.7	4.21%
21-day Voronoi		76.9	3.95%
7-day TO	79.1	79.6	0.63%
14-day TO		79.3	0.25%
21-day TO		73.8	6.93%
Strut Thickness (μm)			
7-day Voronoi	190	231.46	19.67%
14-day Voronoi		233.38	20.49%
21-day Voronoi		229.12	18.67%
7-day TO	200	200.79	0.39%
14-day TO		210.70	5.21%
21-day TO		225.71	12.08%
Trabecular Separation (μm)			
7-day Voronoi	489	521.31	6.39%
14-day Voronoi		546.49	11.10%
21-day Voronoi		551.52	12.02%
7-day TO	554	561.16	1.28%
14-day TO		603.16	8.50%
21-day TO		588.79	6.09%

Dynamic Mechanical Analysis

During the mechanical testing, some of the 7-day Voronoi scaffolds experienced data points of structural failure, which resulted in their exclusion from further analysis (n = 2). To get a comparative analysis on whether time and geometry affected storage modulus, from the remaining data points, a storage modulus average was taken at 2% strain since all scaffolds recorded measurements at this strain. For both geometries, the average storage modulus decreased between 7-, 14-, and 21-day culture (Table 2), and generally decreased for each scaffold as oscillation strain increased (Figure 11). The stiffest storage modulus was recorded by a 7-day Voronoi scaffold (2.05 MPa). To identify significance on seeded (n = 3/geometry and days cultured) and non-seeded scaffolds (n = 1/ geometry and days soaked), a three-way ANOVA test was performed and revealed a significant difference in stiffness between geometries ($p = 0.02071$), shown in Figure 12. Additionally, a two-way ANOVA test, excluding non-seeded scaffolds, was conducted and confirmed a significant relationship with scaffold geometry ($p = 0.03778$). A post-hoc Tukey HSD test revealed no significant interaction between the Voronoi and Truncated Octahedron geometries as a whole and found no significance between the interactions of geometries and culture times.

Table 2. Storage modulus of the geometries at 2% oscillation strain for 7, 14, 21-day cultures (mean ± SD)

	Geometry	Day	n	Stiffness (MPa)
Seeded	Voronoi	7	3	1.41 ± 0.62
		14	3	0.79 ± 0.42
		21	3	0.57 ± 0.27
	Truncated Octahedron	7	3	0.62 ± 0.04
		14	3	0.52 ± 0.23
		21	3	0.50 ± 0.15
Unseeded	Voronoi	7	1	0.63
		14	1	1.18
		21	1	0.69
	Truncated Octahedron	7	1	0.61
		14	1	0.42

		21	1	0.39

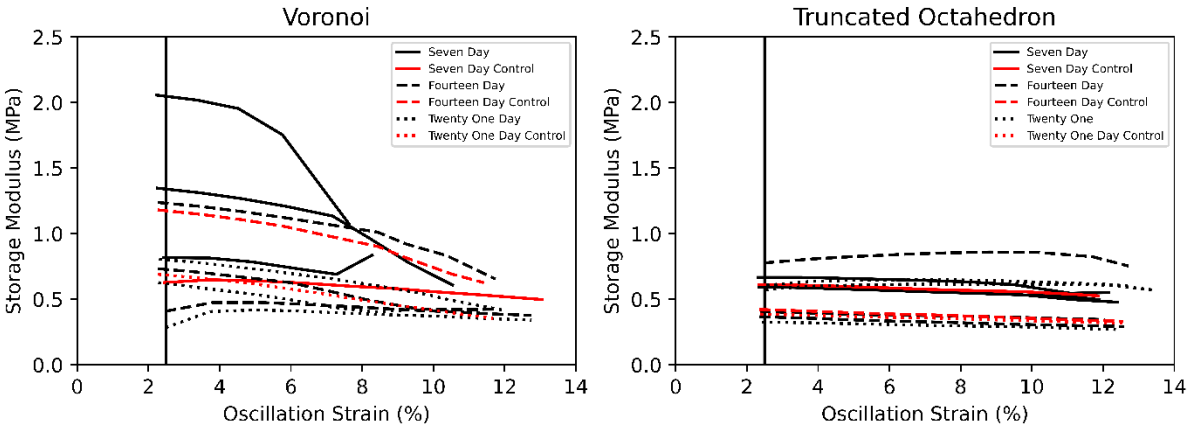

Figure 11. Storage modulus (MPa) vs. oscillation strain (%) for seeded Voronoi and TO scaffolds at 7-, 14-, and 21-day culture timepoints. Storage modulus observed at 2% oscillation strain was utilized for quantitative comparison.

When observing the highest storage moduli (2.05 MPa) at 2% strain, the Voronoi scaffold exhibited the largest peak at 7-day culture. In contrast, the TO scaffold reached its peak storage modulus at 14-day culture, measuring 0.860 MPa at 8.8% oscillation strain. For loss modulus, the 7-day Voronoi scaffolds showed a steady trend increase with oscillation strain (Figure 13), reaching a maximum of 0.121 MPa, which corresponded to a higher tanδ value in comparison to the other Voronoi replicates and TO scaffolds (Figure 14). On average, the Voronoi geometry exhibited a higher tanδ compared to the TO, indicating greater damping behavior. This suggests that the Voronoi structure is more energy-absorbing, making it more viscoelastic and dissipating energy under dynamic mechanical loading. (Figure 14).

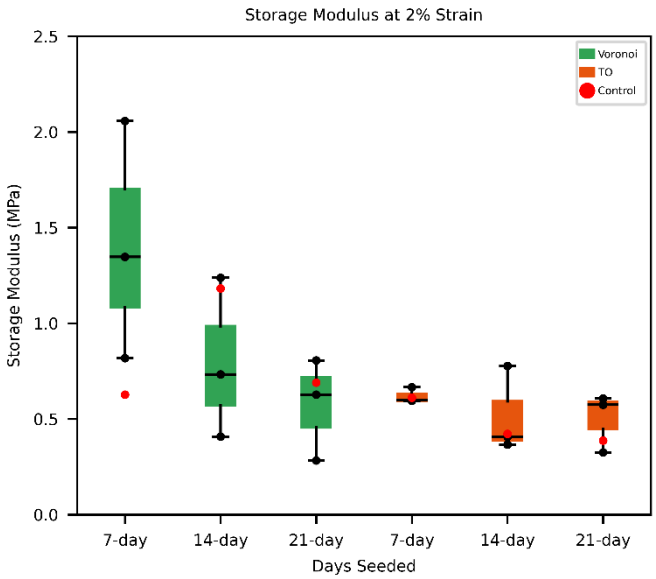

Figure 12. Storage modulus of the Voronoi and Truncated Octahedron geometries at 2% oscillation strain for 7-, 14-, and 21-day cultures. Outlier significance is presented by α=0.05; no moderate or extreme outliers were identified.

Despite the range of reported E' and tanδ within 7-, 14-, and 21-day culture groups at 2% oscillation strain, no moderate and extreme outliers outside ±2 standard deviations from the mean were detected. Figure 12 shows the spread of the data at 2% oscillation strain, with individual data points and control labeled.

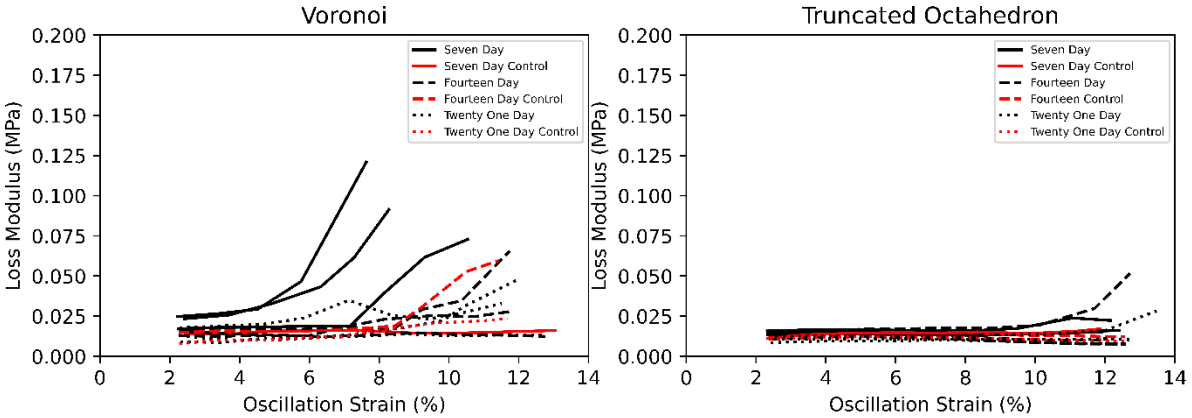

Figure 13. Loss Modulus (MPa) vs. oscillation strain (%) for Voronoi and Truncated Octahedron scaffolds

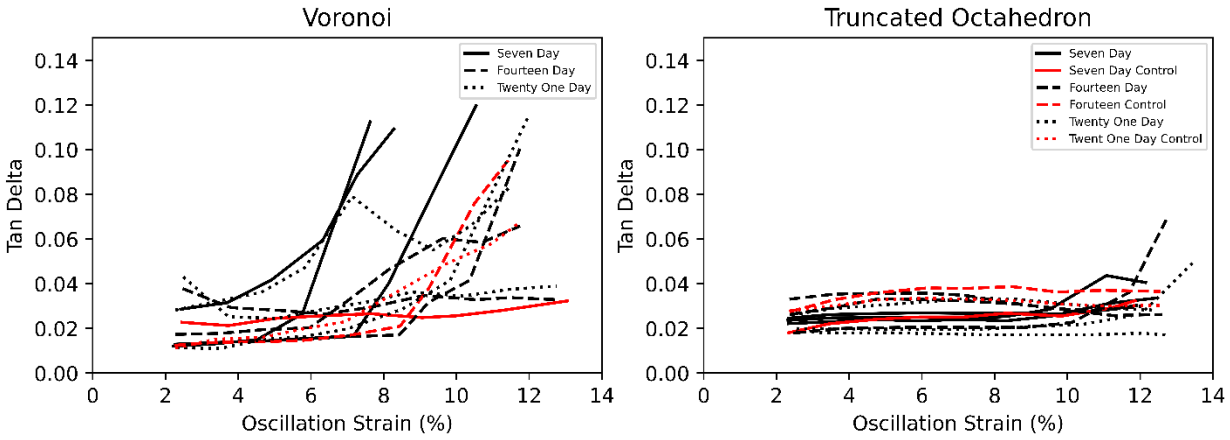

Figure 14. Tan(delta) vs. oscillation strain (%) for Voronoi and Truncated Octahedron scaffolds

Scanning Electron Microscopy

To better understand the observed decrease in storage modulus for the Voronoi scaffolds and the lack of increase in the Truncated Octahedron (TO) scaffolds, SEM imaging was performed, revealing visual microstructural changes within each environment. SEM imaging at up to 100× magnification enabled the visualization of individual photopolymerized printing layers, as shown in Figure 15. These clearly defined layers, and any disruption in their pattern, allowed for the qualitative assessment of cell adhesion, mineral deposition, and potential scaffold degradation. In Figure 15 and 17, mineral formation on the surface of the photopolymerized layers provides qualitative evidence of cell adhesion. Additionally, Figure 15A and 15B reveal distinct disruption in scaffold layers across multiple regions, suggesting that cellular activity may have contributed to localized degradation. In Figure 16, a cellular cluster exhibiting dendritic morphology further supports the presence of adherent cells and ongoing mineralization. Figure 18 displays the energy-dispersive X-ray spectroscopy (EDX) spectrum, with peaks corresponding to elemental composition during scanning. Overall, SEM served as a valuable tool for qualitatively evaluating cell behavior, matrix deposition, and scaffold integrity in response to different culture conditions.

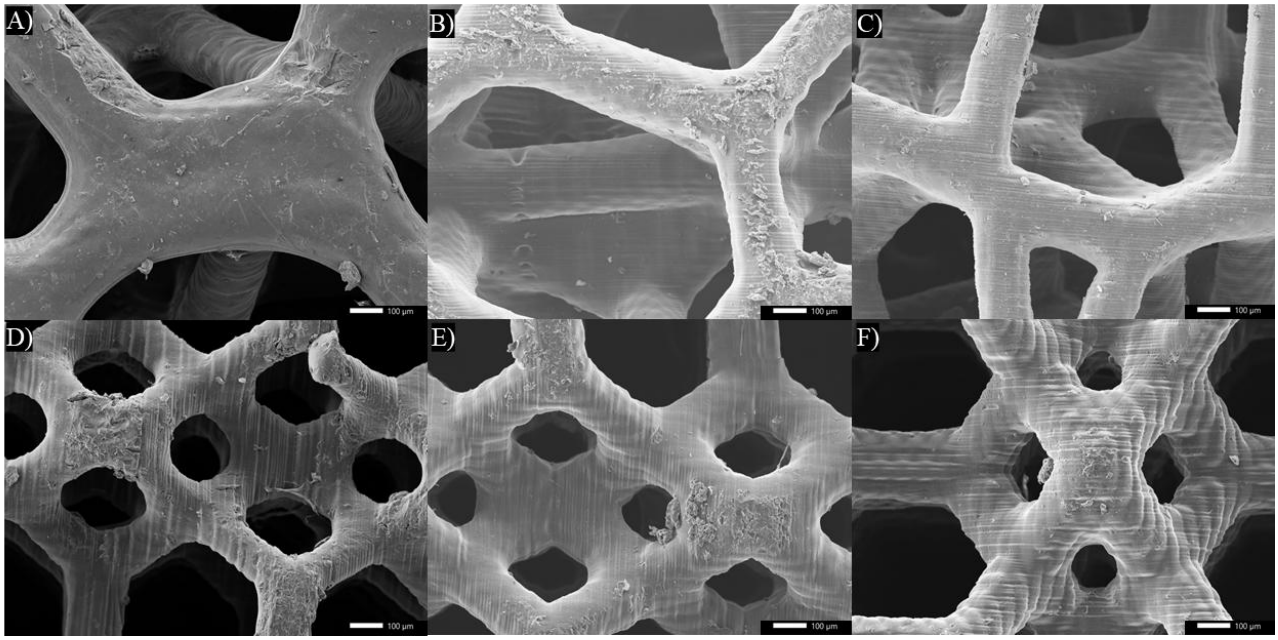

Figure 15. SEM images of Voronoi and TO scaffolds at 100X magnification. A) Voronoi 7-day culture. B) Voronoi 14-day culture. C) Voronoi 21-day culture. D) TO 7-day culture. E) TO 14-day culture. F) TO 21-day culture.

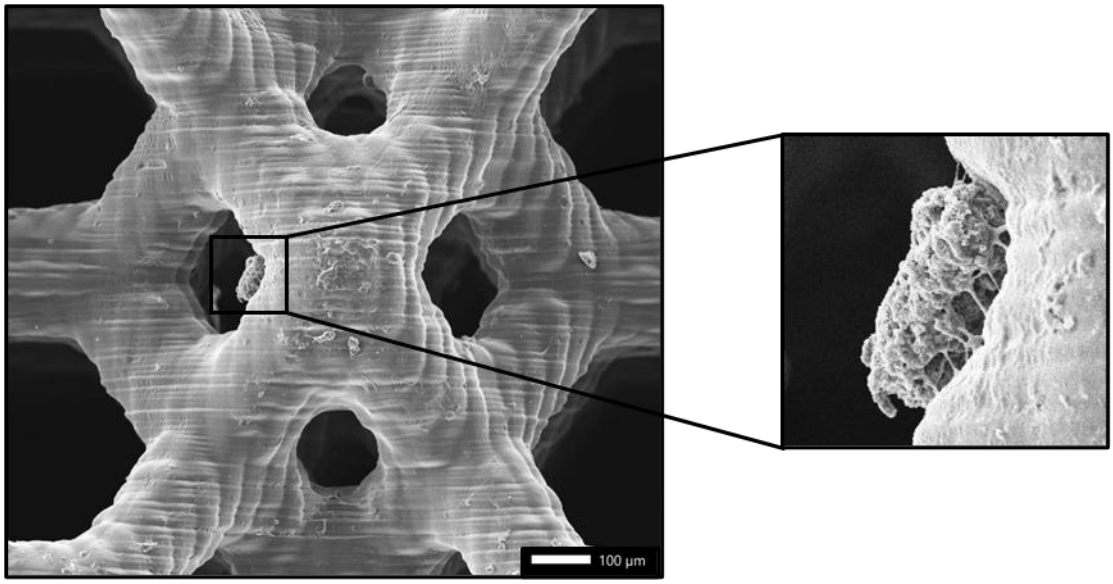

Figure 16. Zoomed SEM image of 21-day TO culture extracellular matrix displaying dendrite characteristics

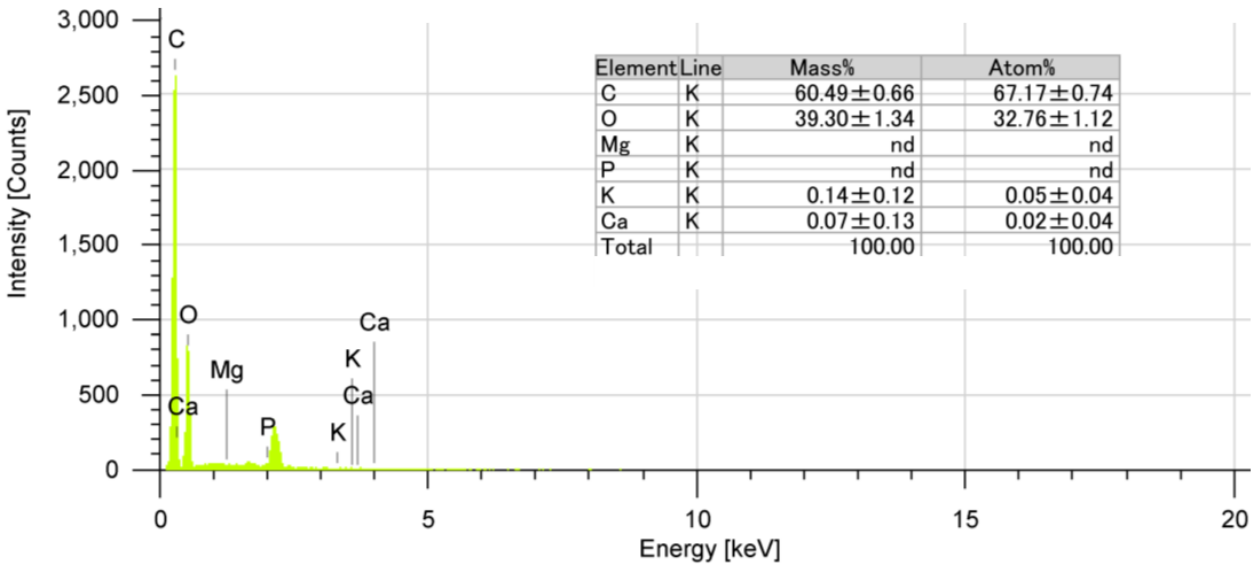

Figure 17. Elemental composition analysis via SEM-EDX (counts vs. photon energy in keV) on 14-day Voronoi scaffold

3.5 Discussion

This study aimed to enhance and explore the influence of human osteoblast cells on 3D-printed geometries in the context of tissue engineering, with an emphasis on structural and mechanical properties post-seeding and long-term culture. Furthermore, this study was the first to mechanically and qualitatively characterize our novel 3D-printed scaffolds seeded with human osteoblasts to assess the ability of the *in vitro* model to replicate the human bone microenvironment. Our results indicate that scaffold geometry has a profound impact on cell morphology and cell behavior related to mechanical properties, which varied in storage modulus in comparison to the study conducted by Choi et. al.

μCT was used to assess scaffolds (n = 1/geometry/culture time) and the influence of osteoblast presence and culture time related to CAD parameters. For Voronoi scaffolds, the ideal porosity was 80%; however, with cell incidence, the Voronoi scaffolds obtained a larger percentage difference range, suggesting higher amounts of early ECM deposition and a decrease in deposition over time, causing an increase in porosity. With μCT data, there is correlating

evidence that with lower porosity scaffolds, higher storage modulus can be achieved, which is evident in the 7-day Voronoi scaffolds Figure 12 and Table 1. Additionally, in later cultures, the Voronoi scaffolds show an increasing trend in porosity, indicating potential degradation of the structure over time. Furthermore, the μCT data reveal that trabecular separation increases over culture time, which could play a role in the decrease of storage modulus in the Voronoi scaffolds. For trabecular separation, Voronoi scaffolds saw a direct relationship between porosity and separation. Opposite to Voronoi, TO observes a decrease in porosity over time, suggesting mineral deposition and shares a reverse relationship with strut thickness, which increases over culture time. Since all scans had an n = 1, concluding that the hFOBs had a significant effect on the porosity, strut thickness, and separation is difficult; however, trends in the data suggest some differences from the ideal print geometries.

With the limited number of samples (n = 3/geometry/culture time) available for mechanical testing, there were no significant changes in storage modulus with respect to geometry and time cultured. The Voronoi scaffolds demonstrated the highest storage modulus among 7-day seeded scaffolds, which follows similar mechanical trends from previous studies conducted by Choi et al. Furthermore, 7-day storage for both Voronoi and TO has been consistent with the study conducted by Choi et. al. Voronoi scaffolds did experience decreased storage modulus over time, which may be attributable to the static culture environment the scaffolds experienced for a longer duration. These findings can correlate with the uCT data, where 7-day scaffolds saw lower trabecular separation compared to the other Voronoi and TO scaffolds, which might indicate early ECM deposition and encourage a higher storage modulus compared to other scaffolds. Compared to TO, the Voronoi scaffold had a higher increase in tanδ when the oscillating strain was increased. This relationship provides evidence that the Voronoi structure is more viscous and does not store energy

but instead disperses energy better. TO, on the other hand, shows a tight tanδ measurement as strain increases regardless of culture time, which would suggest that the TO geometry is characterized to store energy rather than dissipate it. Furthermore, since TO is a more uniform structure with the same repeating unit factor, and it has a lower variance compared to Voronoi, the storage modulus remained relatively consistent during long-term culture. A limitation of the DMA testing was the number of scaffolds per group and culture time (n = 3), which led to no significant difference between those interactions. Future studies should conduct a power analysis to determine the appropriate number of scaffolds required for statistical significance, along with including an equal amount of unseeded control to better isolate the effects of human osteoblasts on the scaffold mechanical properties.

Since cell proliferation data was difficult to obtain due to technological difficulties (equipment failure, maintenance issues, etc.), and the mechanical characterization over time did not follow our hypothesis, SEM was used to qualify cell behavior for this study. Figure 15B is a Voronoi 14-day scaffold that exhibits evidence of mineral deposition and degradation, where the protrusion presents ECM being laid down and the photopolymerized layers being below it. Furthermore, Figure 15A and Figure 15B can be assessed qualitatively to reveal surface degradation in the form of exposed underlying material, with imperfect, rough, and rigid sections visible. TO scaffolds also offer visible ECM deposition at all three time points, where deposition morphology of apparent individual cells mimics a more dendritic phenotype. Figure 16 shows a close-up image of the 21-day TO scaffold, where cells laid down ECM on a concave surface, exhibiting dendritic attachment to the scaffold. A potential limitation to using the SEM is the sensitivity of the detection limit of the elements. Since the elemental map was analyzed under 30x magnification, there might have been a broader surface area that was not able to be extracted for

element presence. This could be mitigated by increasing the magnification and taking localized images where ECM is visible on the macro-scale and then running an elemental analysis. Since the scaffolds are primarily made out of polymers, carbon, and oxygen express the most mass percentage. With the benchtop SEM having a detection limit of ≥1% wt, elements detected at or below a 1% wt. might not be reliable; therefore, analysis done at 30X magnification might not be able to quantify ECM tissue composition on the scaffolds as is represented in Figure 16. Additionally, the EDX energy axis on the spectrum should be focused to improve qualitative peaks and enhance the mass percentage for elements of interest.

4 Specific Aims 2

4.1 Preamble

The following chapter is in collaboration with the Roberts Glyco-Diversity Lab to collect preliminary data for future breast-to-bone metastatic studies. Future work will include collaboration with the Whittington Lab to introduce a transwell-adapted scaffold to be mechanically characterized in co-cultured environments.

4.2 Introduction

The primary objective of this study is to characterize the viability, proliferation, and mechanical properties of osteoblasts when co-cultured with extracellular vesicles (EVs) and breast cancer cells within a simulated metastatic bone niche. This will utilize the scaffolds developed in Aim 1 and apply dynamic mechanical analysis (DMA) to evaluate biomechanical outcomes. To assess osteoblast health and function, viability, proliferation, and gene expression assays will be performed to determine the impact, positive or negative, of co-culture conditions. The central hypothesis is that introducing breast cancer-derived EVs into co-culture with human osteoblasts will enhance osteoblast proliferation and viability. Furthermore, it is anticipated that direct co-culture with breast cancer cells will lead to improved mechanical properties of the scaffold and upregulation of osteoblast-specific gene expression.

4.3 Methods and Materials

Media Concentration Viability

To establish an optimal co-culture environment for both the breast cancer cells and 1.19 hFOBs, a 2D cell viability assay was performed for 24-, 48-, and 72-hours. 1.19 hFOBs were seeded in a 24-well culture plate (Nunc, ThermoFisher) at a cell density of 0.05×10^5 (n = 3/ media condition). The concentration at which they were tested was full breast cancer or non-cancerous media (100%), equal parts of breast cancer or non-cancerous media with osteogenic media

(50%/50%), and full osteogenic media (100%) as a control. The following are the different culture media relative to the cell type: MDA-MB-231 & MDA-MB-468 (DMEM + 1000x Glutamax + 10% FBS, ThermoFisher), T47D (RPMI + Insulin + 10% FBS, ThermoFisher), MCF10A (DMEM F-12 + EGF + Insulin + Hydrocortisone + Cholera Toxin + Penicillin/Streptomycin + 5% HS), and osteogenic (DMEM F-12 + G418 + 10% FBS).

Once the final 0.05 x 10^5 cell densities are obtained, 1 ml of each testing condition media was added to each well. After each time-point, the testing condition media was carefully aspirated, washed with PBS (1x, pH 7.4), then 300 µL of LIVE/DEAD™ Viability staining reagent was added and left to incubate at room temperature for 30 minutes. Next, the wells were examined using a fluorescence microscope (Discover Echo Revolution) with a FITC and TRITC filter to assess live and dead cells, respectively. Five different regions of interest (ROI) were determined by splitting up the well into four equal quadrants to represent four ROI, and the fifth ROI was chosen to be in the middle of the well, but if no cells were present, then an image was taken directly above or below the center (Figure 18).

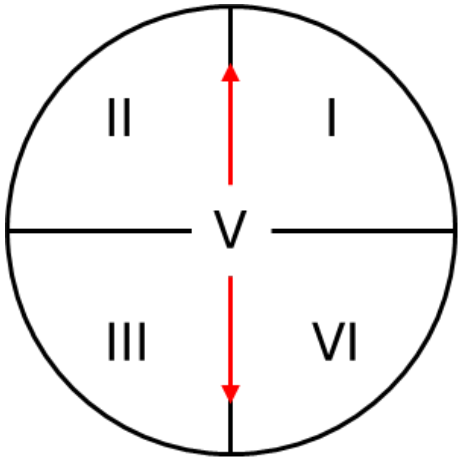

Figure 18. Visual representative of five ROIs in a culture well

Following the image collection, images were imported into a Python code that converts merged images into a JPG to register as an RGB image, so a live and dead cell quantification macro from Allevi Systems can be used in ImageJ.

Extracellular Vesicle Exposure Viability

To better understand the roles and influence that EVs have on the bone environment, a similar 2D viability assay compared to media concentration was conducted on EV exposure. 1.19 hFOBs were cultured out using a specific double-time (36 hours) to achieve a cell density of 0.5 x 10^5 (n = 3/group). EVs from either ER+ or TNBC cells were seeded with the osteoblasts and left to culture for 24 and 48 hours. Each well was conditioned with 1 ml of a 50%/50% (BC/OG) media concentration and had osteogenic control. After each time point, the testing media was aspirated and followed the same steps for sample preparation and imaging as mentioned in the 2D media concentration viability section.

Osteoblast Proliferation

To assess the effects of EV exposure on an indirect measurement of proliferation, four wells of a 24-well plate were seeded with 1.19 hFOB and cultured until a confluent monolayer was created. Once the monolayer formed, a scratch was made by a P200 tip. Released cells were aspirated and underwent a PBS (1x, pH 7.4) wash. After the scratch was washed, 1 ml of fetal bovine serum-free conditioned medias were added. The following media concentrations were: 50%/50% osteogenic/EV-conditioned (MDA-MB-468) breast cancer, 50%/50% osteogenic/breast cancer without EVs, and control osteogenic (100%) media were added to each well (n = 1/group). Cells were incubated under normal body temperature parameters, and images were taken every 6 hours. Researchers calculated area closure using a microscope annotation tool on the Rebel Microscope.*Organoid Co-Culture*

Prior to seeding, all Voronoi scaffolds were sterilized with 70% ethanol and placed into a biosafety cabinet. Unseeded scaffolds underwent an additional sterilization process of 70% ethanol wash for an hour at room temperature. After sterilization, three 30-minute static washes of phosphate-buffered saline solution (1x PBS, pH 7.4) were performed. Following the PBS washes, a final 30-minute wash of complete osteogenic media supplemented with DMEM F-12 (ATCC), 10% FBS (ATCC), and 3 ml of 20X G-418 (Thermo-Fisher) was carried out to ensure all traces of ethanol were removed.

Voronoi scaffolds adapted from Aim 1 to be compatible with a transwell insert, were utilized as rectangular prisms (10 x 10 x 3 mm) for co-culture. These scaffolds were seeded with a ratio of cell density (1:3.33) proportional to their new height. 7.5×10^3 of human osteoblasts (1.19 hFOB) and human breast cancer (T47D) cells were seeded into each scaffold and left to attach for 15 minutes at 37℃, 5% CO2, and flipped to ensure the cells were properly attached. Once a full 30 minutes had elapsed, 1 ml of 50%/50% breast cancer and osteogenic media was added. Seeded scaffolds were left to culture for 4 (n = 6, one control) and 7 (n = 6, one control) days under static culture. Following each culture time, scaffolds were immersed in 1 ml of 10% buffered formalin for five minutes. The scaffolds were washed with 1X PBS for two minutes and then immersed in another 1 ml of 10% buffered formalin for 20 minutes to fix the cells. After fixation, scaffolds were rinsed with 1X PBS for one minute, twice, to remove excess formalin. Before seeding, cells were stained with cell trackers to differentiate the cell types. Osteoblasts and T47D were stained with CellTracker™ Green CMFDA and CellTracker™ Red CMTPX, respectively.

Organoid Osteocalcin Production

To identify whether co-culturing human osteoblasts with T47D breast cancer cells would affect the concentration of osteocalcin, a non-collagenous protein, a human osteoblast ELISA (Invitrogen) assay kit was used. After each co-culture time point (4- and 7-day), scaffold waste media was aspirated and transferred into a protein low-binding tube (Eppendorf) and rapidly cooled by dipping it into liquid nitrogen to avoid ice crystallization. Media samples were thawed at 37℃ and were ready for analysis. Following the protocol, samples were then analyzed using a microplate reader at 450 nm to calculate the absorbance. Absorbance values were then input into a four-parameter logistic curve software to determine the expression of osteocalcin concentration (ng/ml). Statistical analysis was performed in Python using one-way ANOVA to determine significant osteocalcin concentration increase between 4- and 7-day co-cultures.

Breast-to-Bone Organoid DMA

To mechanically characterize the co-cultured scaffolds until failure, the same benchtop DMA from Specific Aim 1 was performed on the 1.19 hFOBs and T47D seeded (n = 5/geometry for 4- and 7-day cultures) and unseeded (n = 1/geometry for 4- and 7-day cultures) scaffolds through cyclic compression loading using a strain sweep to analyze how the cell types and culture time impacts the metastatic organoid's storage modulus (E'), loss modulus (E"), and loss factor (tan δ). The strain sweep was conducted at a frequency of 0.1 Hz with an initial dynamic amplitude of 0.2 mm (6% strain) and increased at a step size of 0.1 mm until a 1 mm dynamic amplitude (30% strain) was achieved. All samples were submerged in phosphate-buffered saline (1x PBS, pH 7.4) at 37 ℃ (Figure 11).

Statistical Analysis

Mechanical data was analyzed using a two-way ANOVA test in Python to identify significant differences between time-cultured and dynamic mechanical properties. An additional Tukey HSD post-hoc analysis was performed to establish significance between individual groups ($\alpha = 0.05$). A z-score normalization analysis was also carried out in Excel and Python using a threshold of ±3 standard deviations from the mean to identify any potential outliers in the mechanical testing data. An effective size calculator and power analysis were used to calculate the sample size needed to achieve significance.

4.4 Results

Media Concentration Viability

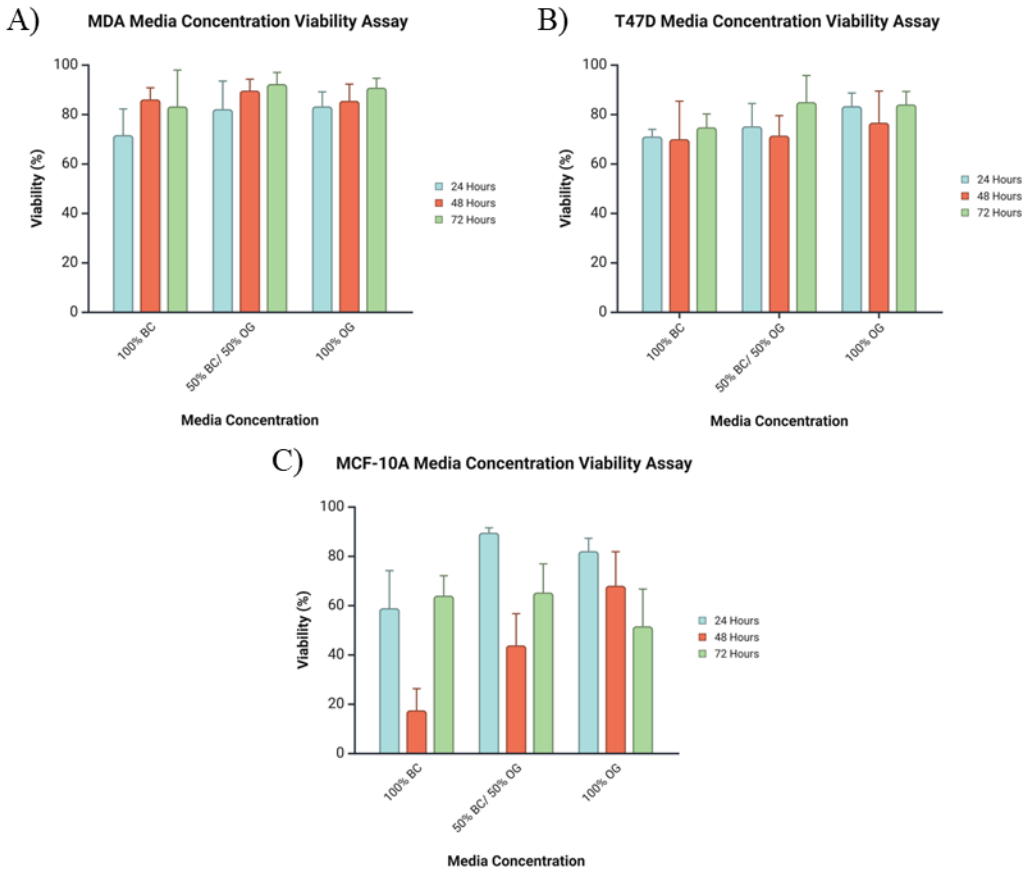

Figure 19. Osteoblast viability after culturing in different breast cancer media concentrations (100% BC, 50%/50% BC/OG, and 100% OG media). A) OB viability in MDA-MB complete media. B) OB viability in T47D complete media. C) OB viability in MCF-10A (non-cancerous) complete media.

Following 72 hours of culture, media derived from two different breast cancer cell lines, MDA-MB-231 (TNBC) and T47D (ER+), as well as normal breast tissue, had varying effects on the viability of human osteoblasts (Figure 19). In the MDA condition, osteoblast viability steadily increased over time across different media concentrations. Although two-way ANOVA revealed no statistically significant differences across time or concentration, viability was highest at the 72-hour mark. Based on this trend, the 50% MDA/50% osteogenic media concentration was selected for further experiments, as it balances both tumor-derived and osteogenic environments to better mimic the bone metastatic niche. Similarly, in the T47D condition, viability decreased at 48 hours across all concentrations, followed by a recovery at 72 hours that exceeded baseline levels at 24 hours. Again, two-way ANOVA showed no significant differences between concentrations, but the 50% T47D/50% osteogenic media condition was deemed optimal due to the observed peak in viability at 72 hours.

To get a perspective on non-tumorigenic tissue, MCF10A viability was assessed, and showed mixed takeaways from the assay. For 100% MCF10A media at 48 hours, it was significantly lower than 100% osteogenic media at 48 hours ($p < 0.0.05$). Since the other viability assays showed higher viability in the 50% BC/ 50% OG and the 100% osteogenic media than the 100% breast cancer results, those results were excluded, and another two-way ANOVA was run, which showed no significant interactions with each other at later time points. Following the same trend as the previous viability assays, the 50% 10A/ 50% OG was selected as the ideal environment for later experiments.

Extracellular Vesicle Exposure Viability

After establishing the ideal environment for supporting osteoblast viability while incorporating elements of the bone metastatic niche, the next step was to evaluate the influence of extracellular vesicles (EVs) on osteoblast viability. Similar to the media concentration experiments, osteoblasts were cultured and then exposed to EVs in a 50% breast cancer-derived EVs/50% osteogenic media mixture for 24 and 48 hours to assess potential changes in viability (Figure 20). Osteoblasts exposed to MDA-MB-231 EVs exhibited a lower percentage of viability compared to both the 50%/50% media and the osteogenic control; however, two-way ANOVA revealed no statistically significant differences, indicating that MDA-MB-231 EVs did not significantly impact osteoblast viability at either time point. Similarly, osteoblasts exposed to MDA-MB-468 EVs showed viability levels comparable to those in the 50%/50% media and osteogenic controls. This similarity, confirmed by two-way ANOVA, demonstrated that MDA-MB-468 EV exposure also had no significant effect on osteoblast viability.

For T47D (ER+) exposure, a significant difference in viability ($p < 0.05$) was detected between culture times, with decreasing viability with culture time. As such, T47D exposure has a negative impact on osteoblasts' viability over time (Figure 20). A Tukey HSD post-hoc test revealed that there was no significant interaction between specific viability measurements (i.e. 100% EV 24 hours vs 100% OG 48 hours).

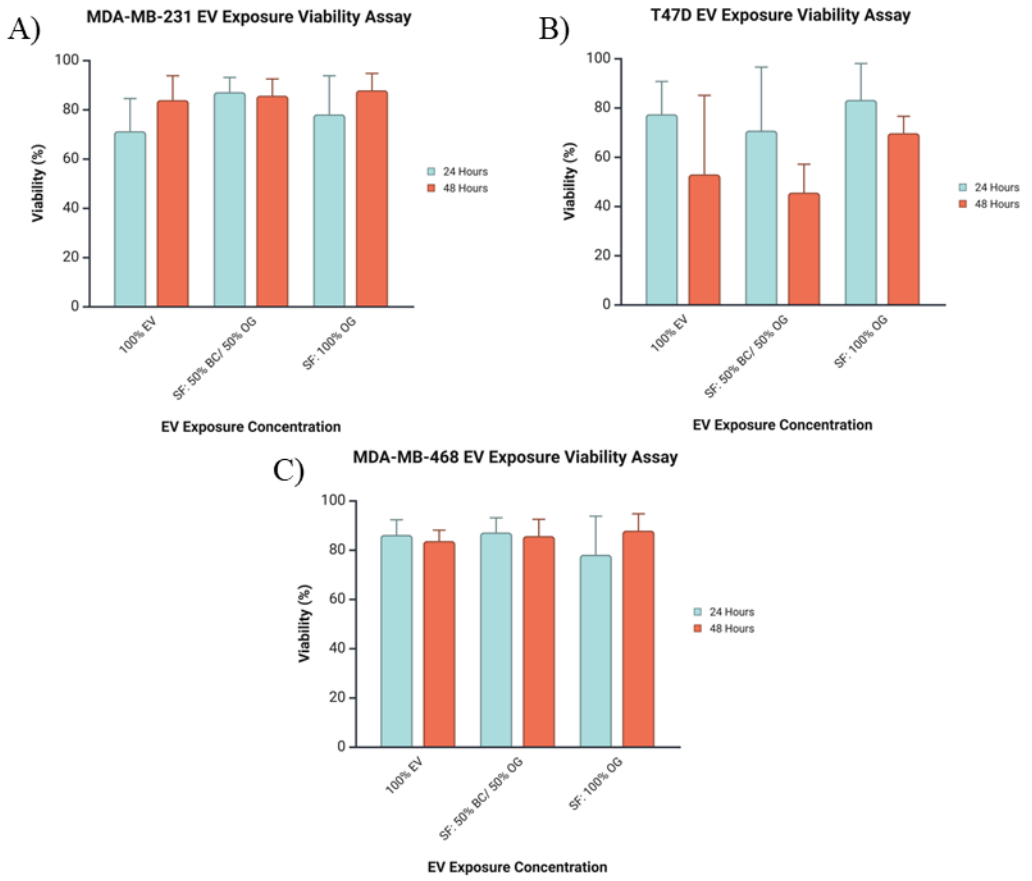

Figure 20. Osteoblast viability after co-culturing in EV-exposed breast cancer media (EV-exposed, Serum-Free 50%/50%, and 100% OG media). A) OB viability in MDA-MB-231 EV-exposed media. B) OB viability in T47D EV-exposed media. C) OB viability in MDA-MB-468 EV-exposed media.

Osteoblast Proliferation

To assess the proliferative response of osteoblasts exposed to breast cancer-derived EVs, a preliminary scratch assay (n = 1) was conducted. The assay revealed that there was an increase in the rate of gap closure in osteoblasts treated with MDA-MB-468 EVs compared to controls (Figure 21), suggesting an indirect measurement of enhanced proliferation. Although statistical significance cannot be determined due to the small sample size, the %age of gap closure was greater when osteoblasts were conditioned in breast cancer EVs (Table 3). Additionally, exposure to triple-negative breast cancer (TNBC) EVs resulted in more uniform qualitative gap closure by 12 hours (Figure 22). By 18 hours, no visible scratches remained in either condition; however, the

osteogenic control had not yet surpassed 80% confluency. By 24 hours, a monolayer of osteoblasts had been reestablished in both conditions.

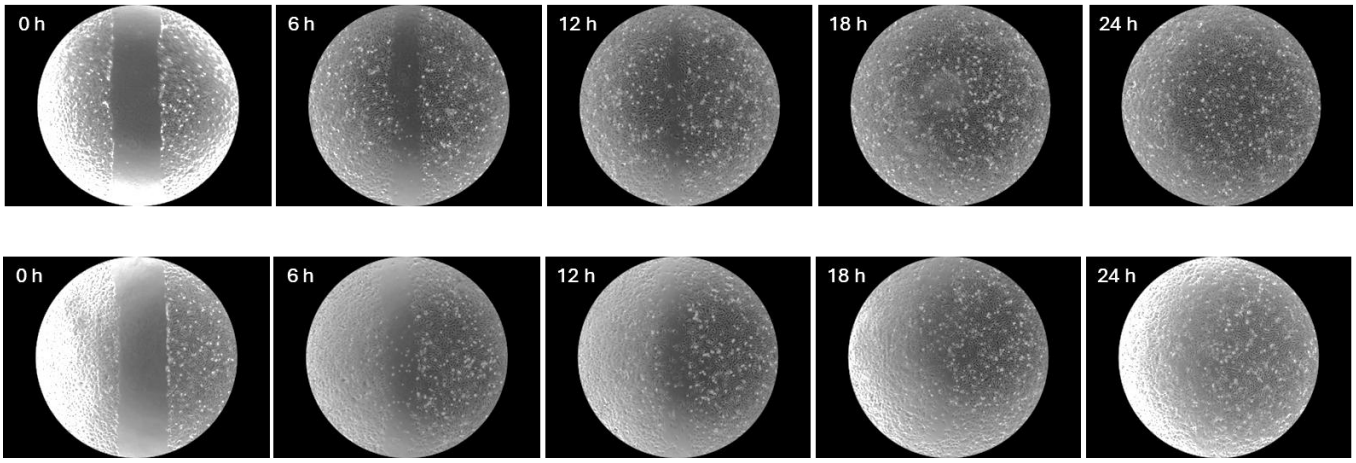

Figure 21. Scratch Assay results between 0 and 24 hours at a 6-hour increment. The top images represent 1.19 hFOB in MDA-468 EV conditioned media, and the bottom images represent the osteogenic control.

Table 3. Effects of MDA-468 Extracellular Vesicles (EVs) exposure on area closure after 6-hr increments for 24 hrs.

	Time Point (Hrs.)	0	6	12	18	24
MDA-468	Area (mm^2)	1.518	0.776	0.148	0	0
	Scratch Closure (%)	0	48.88	90.25	100	100
100% OG	Area (mm^2)	1.554	0.849	0.346	0	0
	Scratch Closure (%)	0	45.37	77.73	100	100
50%/50%	Area (mm^2)	1.670	0.863	.314	0	0
	Scratch Closure (%)	0	48.32	81.20	100	100

Organoid Osteocalcin Production

When assessing 4- and 7-day co-cultured media in the human osteocalcin ELISA assay, a standard curve was created using 4PL to create a standard curve with an R^2 value of 0.993. In Table 4, there is a quantitative increase between 4- and 7-day culture. When running a one-way ANOVA, there was no significance observed between the two culture times. Additionally, 7-day

culture has a larger standard deviation than 4-day culture, which indicates a larger spread of concentrations and a need for more samples in future studies to make conclusions. In Figure 22, the correlation matrix shows a moderate positive linear relationship (r = +0.45) between the osteocalcin concentration of 4- and 7-day cultures, which reveals that osteocalcin levels tend to be higher at a longer culture duration. This can also be visually seen in Figure 23, where the 7-day has an increase in concentration compared to the 4-day concentrations.

Table 4. Expansion of osteocalcin measurements after 4- and 7-day co-culture

	Osteocalcin Concentration (ng/ml)	
	Day 4	Day 7
	62.77	59.11
	58.64	56.66
	60.48	64.46
	62.66	60.64
	58.07	79.79
	55.77	76.51
Average ± STD	59.73 ± 2.75	66.19 ± 9.66

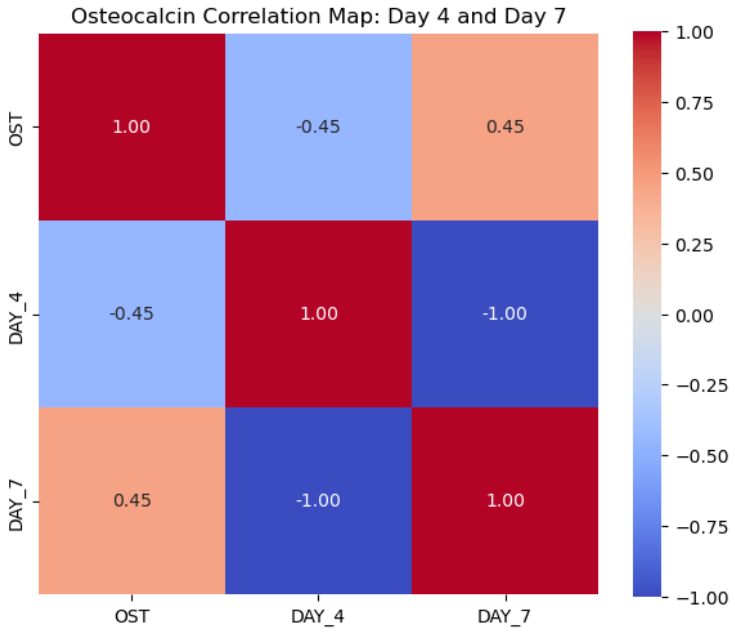

Figure 22. Osteocalcin concentration correlation heat map of 4- and 7-day co-cultured media. The Pearson correlation coefficient is 0.45.

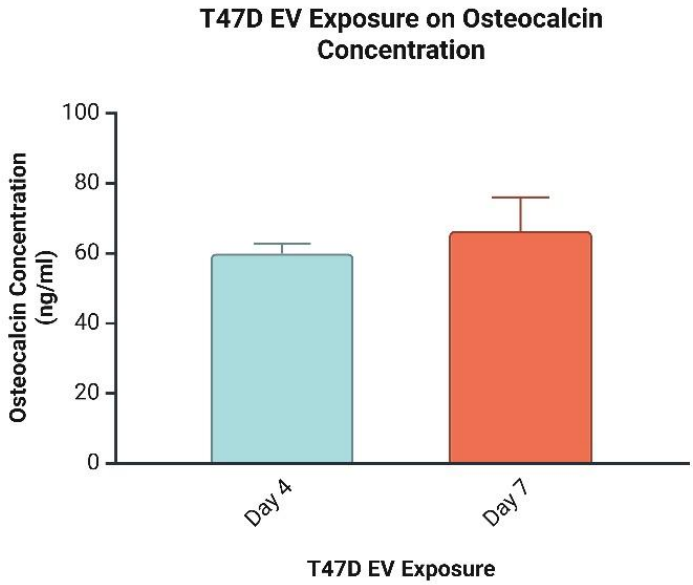

Figure 23. Osteocalcin concentration (ng/ml) after 4- and 7-day co-culture with T47D breast cancer cells and 1.19 hFOB. The calibration curve has an R^2 value of 0.993.

Breast-to-Bone Organoid DMA

Due to the decrease in scaffold height and the greater increase in oscillating strain, the scaffolds for both 4- and 7-day experienced data points of structural failure, which were excluded

from further statistical analysis (n = 12). To get a comparative assessment on whether time affected the storage modulus of the co-culture organoid, average storage modulus data were taken at 19% strain since some scaffolds' first measurements were collected at this strain. For the duration of culture, the average storage modulus increased between 4- and 7-day culture (Table 5), and generally decreased for each scaffold as oscillation strain increased (Figure 24). For the co-cultured scaffolds, the stiffest storage modulus was recorded by a 7-day Voronoi scaffold (0.249 MPa). To identify significance on 4-day (n = 5) and 7-day scaffolds (n = 5), a one-way ANOVA test was performed on the storage moduli of the 19% strain, which revealed no significant difference between 4- and 7-day stiffness. Trends in loss modulus were consistent among the culture times, with a general increase directly related to increased oscillation strains.

Table 5. Organoid storage modulus of the geometries at 19% oscillation strain for 4- and 7-day cultures (mean ± SD)

Geometry	Cell Presence	Day	n	Stiffness (MPa)
Voronoi	Seeded	4	5	0.16 ± 0.024
		7	5	0.19 ± 0.037
	Unseeded	4	1	0.147
		7	1	0.195

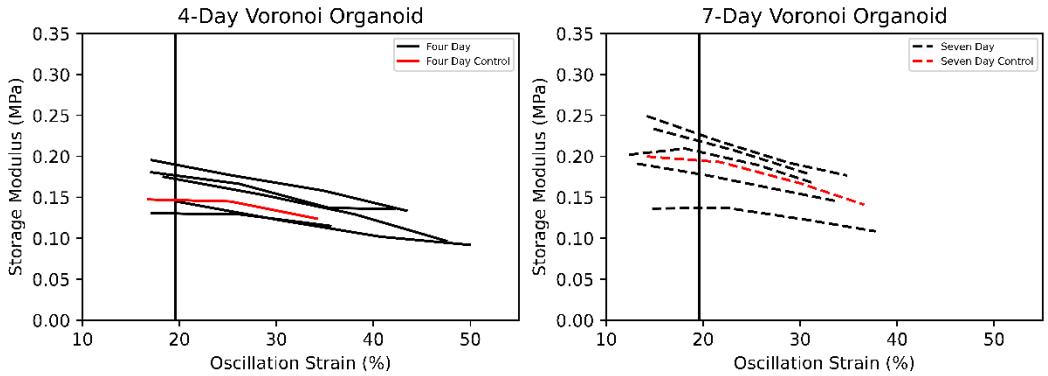

Figure 24. Organoid storage modulus (MPa) vs. oscillation strain (%) for seeded Voronoi at 4- and 7-day cultures. The storage modulus observed at 19% oscillation strain was utilized for quantitative comparison.

When individually observing the highest storage moduli, the peak value was recorded at 0.195 MPa by the 4-day culture at 17% oscillation strain. For loss modulus, 7-day Voronoi saw an increase over oscillation strain (Figure 25), with the highest being 0.257 MPa. Relatively, the loss modulus of the culture times was consistent with each other up to (0.010 MPa < x < 0.026 MPa). Overall, the Voronoi geometry saw a tight tanδ throughout the different culture durations, which suggests similar damping characteristics (Figure 26).

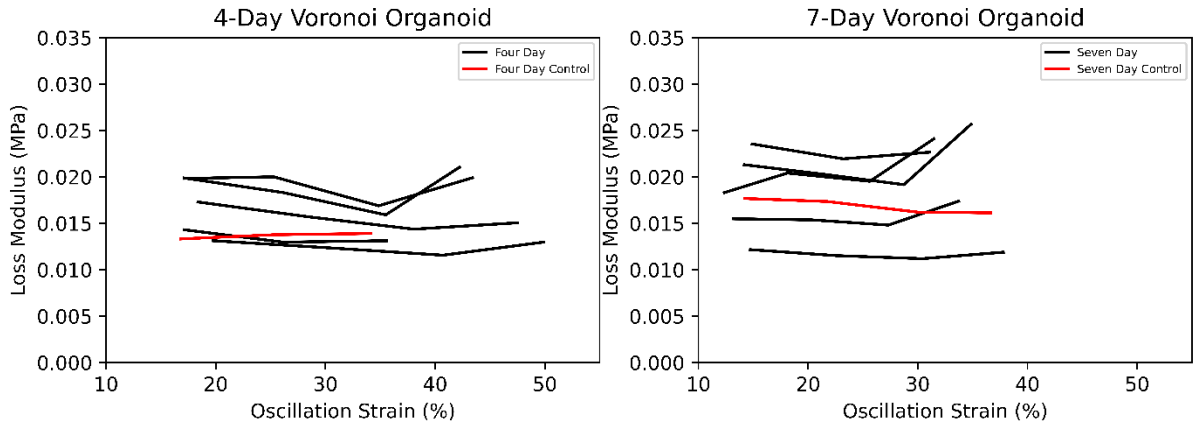

Figure 25. Organoid loss Modulus (MPa) vs. oscillation strain (%) for Voronoi and Truncated Octahedron scaffolds

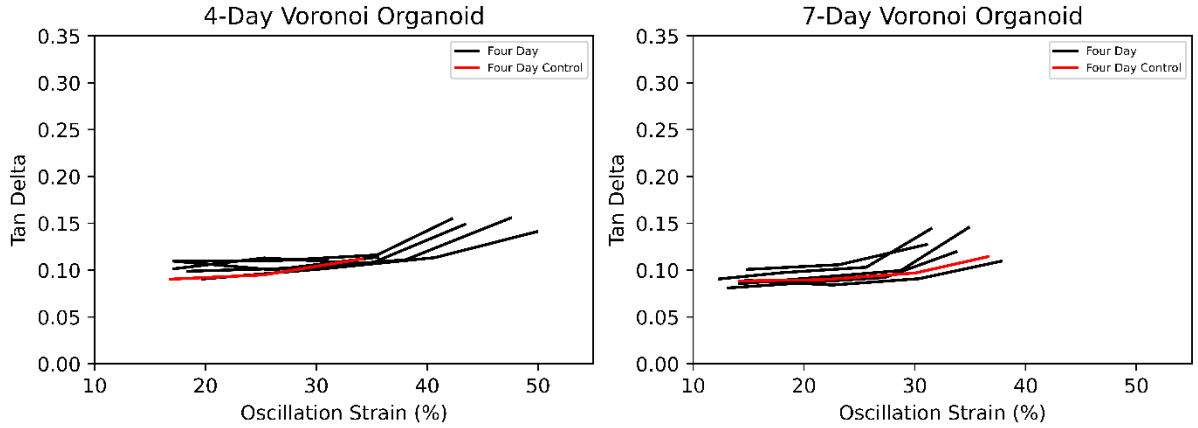

Figure 26. Organoid tan(delta) vs. oscillation strain (%) for Voronoi and Truncated Octahedron scaffolds

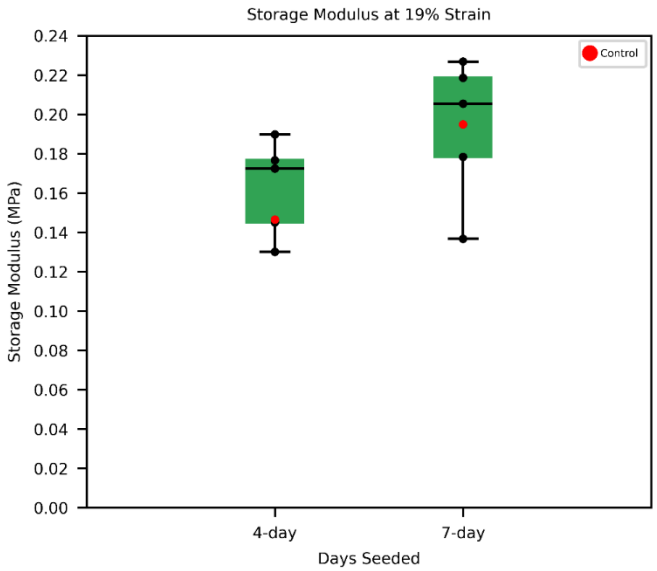

Figure 27. Organoid storage modulus of the Voronoi at 19% oscillation strain for 4- and 7-day cultures. Outlier significance is presented by α=0.05; no moderate or extreme outliers were identified.

Despite the reported E' and tanδ within 4- and 7-day culture groups at 19% oscillation strain, no moderate and extreme outliers outside ±2 standard deviations from the mean were detected. Figure 27 shows the spread of the data at 19% oscillation strain, with individual data points and control labeled.

4.5 Discussion

The media concentration viability assay was used to set the foundation for the other assays in the study, which resulted in 50%/50% breast cancer or breast tissue media and osteogenic media concentration to be the most ideal cocktail since there was no significant difference in human osteoblast viability and better represented the metastatic bone environment where both cell types will be present.

Following the breast cancer EV exposure viability, MDA-MB-231 EVs were revealed to have no statistically significant impact on osteoblast viability. This aligns with literature that reports preferential metastasis of MDA-MB-231 cells[120,121] to the brain, suggesting low to no

interaction between these cell types *in vivo*. Similar results were observed when osteoblasts were exposed to MDA-MB-468. Opposite to the two different MDA cell lines, a significant decrease in osteoblast viability was found with culture time after exposure to EVs from T47D cells ($p < 0.05$), which suggests that these ER+ EVs have a negative influence on osteoblast viability. This decrease in viability may result from the fact that the T47D breast cancer phenotype is linked to breast-to-bone metastasis as its primary location for distant metastasis. A limitation of this viability assay was that the concentration of EV was related to the circulatory system, where there is a diluted concentration of EV, which represents the intravasation aspect of breast-to-bone metastasis. Current and future planned studies are looking at concentrations related to the metastatic bone niche to fully characterize osteoblast viability.

Preliminary proliferation data were collected and revealed that when osteoblast cells were conditioned with EVs, they exhibited more qualitative and uniform closure by hour 12 compared to the MDA control and osteogenic control. However, similar to the EV exposure assays, osteoblasts were conditioned with circulating concentration EVs instead of the bone metastatic environment. Specifically, in the proliferation assay, there was a low sample size ($n = 1$); therefore, quantitative analysis was not performed, and future work should explore an appropriate sample size to analyze the rate of gap closure and utilize a proliferation assay to validate findings. Additionally, the image internals were large, which resulted in valuable information, such as when gap closure was initiated, being lost. Future studies should investigate increasing the time interval size to capture all relevant information. Moreover, future studies should stain the osteoblasts before scratching to calculate the proliferation rate and monitor motility behaviors using an onstage incubator microscope.

Scaffolds used for co-culture DMA testing were organically adapted for transwell inserts to assess migration between a breast cancer to an osteoblast environment. Since 3D-printed co-culture metastatic bone scaffolds have never been mechanically characterized to failure, the smaller scaffolds were adapted for mechanical testing. Similar to Aim 1, a 7-day Voronoi scaffold exhibited the highest storage modulus out of the scaffolds. Storage modulus observed at 19% strain revealed an increased stiffness over time; however, there was no statistical difference detected. Within both culture times, tanδ reveals that it has low variance and exhibits similar values to each other, suggesting that 4- and 7-day co-culture is not enough to determine whether or not time has an influence on energy being stored or dissipated. In Figure 24, the 4-day scaffolds have samples that go past 40% oscillating strain, whereas oscillation strain peaks below 40% strain on day 7. This might suggest that the osteoblast and T47D cells might impact the scaffold's structural integrity over longer culture times (lower strain threshold prior to failure), but future studies should take a deeper dive into this anomaly. A limitation of this experiment is that the loading protocol was not effectively adapted for the smaller scaffolds, leading to premature failure. Further, a limited number of scaffolds were available for testing, so to observe a statistically significant difference in storage modulus between 4- and 7-day culture, a sample size of 18 scaffolds is needed per group (n = 36), based on a subsequent power analysis.

5 Conclusion

5.1 Synthesis

This master's thesis details the development of a human osteoblast-seeded scaffold and a bone metastatic scaffold to investigate stiffness in long-term and short-term cultures, respectively. Mechanical characterization and qualification were conducted using DMA, SEM, and uCT imaging. Two geometries–Voronoi and TO–were mechanically tested to analyze the stiffness of human-seeded scaffolds over 7, 14, and 21 days of culture, revealing decreased stiffness over time. To understand why stiffness decreased, SEM and μCT were utilized to validate the behavior of the scaffolds over time, generating images that support cell adhesion and a decline in structural integrity throughout the duration. Preliminary data on osteoblast viability and proliferation after exposure to breast cancer-derived EVs were collected, confirming evidence of decreased cell viability and increased qualitative growth. Mechanical data on the metastatic niche revealed that there was an increase in scaffold stiffness when osteoblasts were co-cultured with T47D breast cancer cells; however, no statistical correlation was observed. To pair the mechanical characterization of the scaffolds, an osteoblast-specific biomarker assay was performed on the culture media to determine altered protein expression in co-culture, which showed a positive correlation with culture time.

Furthermore, the mechanical characterization of the scaffolds provided insights into where both Voronoi and TO had the higher storage modulus at the first time point (day 7) and a decrease related to time. With long culture, scaffold storage modulus has displayed the lowest stiffness relative to a previous study conducted by Choi et. al. 7-day Voronoi scaffolds presented the highest storage modulus, which follows previous results; however, there was no significant impact on culture time for both geometries. Moreover, statistical analysis revealed that Voronoi scaffolds

exhibited greater stiffness than TO scaffolds, consistent with previous findings involving murine fibroblasts. Additionally, mechanical data revealed that Voronoi had higher tanδ values as oscillating strain increased, which suggests that the Voronoi geometry is more suitable for human osteoblast cell seeding, causing energy to be not stored, but for energy dissipation. Data from uCT suggests a relationship for both geometries that seeded the scaffolds' storage modulus decreases as scaffold porosity increases.

Although preliminary, the breast-to-bone data collected in this study lays the groundwork for establishing an in vitro model to aid future work on investigating other mechanisms that drive breast metastasis. Through the challenges of working with multiple breast cancer cell lines co-cultured with osteoblasts, I have identified an ideal environmental condition that would satisfy both cell types and enable exploration of the influence of breast cancer-derived EVs on osteoblast cell viability and proliferation. Among the three breast cancer cell lines, MDA-MB-231, MDA-MB-468, and T47D, T47D exhibited a significant decrease in osteoblast viability, as determined by one-way ANOVA. This finding aligns with the known tendency that EVs can alter the host environment and are accompanied by the ER+ breast cancer trait that metastasizes to bone. Mechanical testing of co-cultured scaffolds showed an average increase in stiffness at 7 days compared to 4-day culture. However, the 4-day samples withstood higher oscillation strain than the 7-day samples. This yield data suggests that the co-cultured environment may influence structural integrity, a pattern consistent with clinical observations of metastatic bone.

5.2 Future Work

Based on the findings of this thesis, a subsequent study investigating human osteoblast-seeded Voronoi and Truncated Octahedron (TO) scaffolds, as well as co-culture scaffolds, is needed to better understand the mechanobiological and metastatic interactions within these

engineered environments and established human cells. This continuation would include DMA testing of more seeded scaffolds (n ≥ 6/geometry/culture time), along with the same number of saoked unseeded scaffolds (n ≥ 6/geometry/culture time) to give a better representation of the impact of the cells on the scaffold mechanics and potentially detect a significant difference between seeded and seeded scaffolds, in line with the power analysis I performed. Furthermore, future studies should consider increasing the seeding density of cells like Choi et. al. Like the human-osteoblast only scaffolds, full 1 cm^3 scaffolds should be co-cultured with breast cancer cells and osteoblasts (n ≥ 6/ culture time), and additional soaked scaffolds (n ≥ 6/ soaked) should be mechanically tested.

5.2.1 Dynamic Bone Tissue Culture Model

The overarching goal of this thesis was to expand an *in vitro* model that can recapitulate the bone microenvironment and be used to analyze applications like breast-to-bone metastasis. For my portion of the bone tissue culture model, I've completed the long-term culture out to 21 days of two geometries, Voronoi and TO, to investigate if human bone-specific cells impact the stiffness over time by cell adhesion, proliferation, and mineral deposition. I collected mechanical data that will be used to deliberate new approaches, since the scaffolds should be tested to mimic the bone microenvironment.

Since the bone is a dynamic and complex environment that houses multiple cells, there has yet to be a model that effectively replicates those physiological features. The bone tissue model that we have developed and enhanced sets the foundation for the next step, which includes mechanically stimulating scaffolds to better mimic the complexity of bone. Instead of performing culture under static conditions, a perfusion bioreactor should be used to better encapsulate the dynamic characteristics of the bone microenvironment, which puts the samples under some

mechanical stimuli while circulating fresh supplements and removing waste media or cells. With this approach, a more physiological *in vitro* model could be developed.

5.2.2 Breast-to-Bone Metastasis

For this thesis, I collected preliminary data for the mechanical properties of a bone metastatic niche and characterized the viability and biomarker expression of co-culture osteoblasts with breast cancer cells and breast cancer-derived EVs. Metastatic bone is known to be prone to fracture due to metastatic tumors, causing osteolytic and osteoblastic characteristics[105,106]. To understand these mechanical changes and deregulated gene expression associated with the co-culture, larger-scale scaffolds and other biomarkers should be observed. Successful mechanical characterization and gene expressions of co-culture would accurately replicate physiological responses, opening new perspectives for assessing metastatic fracture healing, drug administration, and therapeutics.

Furthermore, I collected preliminary cell viability data, addressing one of the three key mechanisms involved in breast-to-bone metastasis. Future studies should focus on adapting the 3D in vitro model to investigate the extravasation potential of extracellular vesicles (EVs), which may facilitate the migration of breast cancer cells to the bone niche. Given the established role of EVs in mediating intracellular communication and promoting premetastatic niche formation, experiments should also examine how EV exposure time influences both the rate of cellular homing to the bone microenvironment and the expression of metastasis-related hormones and proteins. This future direction could yield critical insights into the additional mechanisms by which breast cancer metastasizes to bone.

6 Appendix

6.1 Appendix A: CV

Edward A. Shangin

edshan20@vt.edu | (804) 982-3401
https://www.linkedin.com/in/edward-shangin/

Education

Virginia Polytechnic Institute & State University (Virginia Tech), Blacksburg, VA
M.S. Biomedical Engineering, May 2025, GPA: 3.85
B.S. Biomedical Engineering, May 2024, GPA: 3.55

Experience

Lab Manager, The Collins Lab, Blacksburg, VA August 2023 – Present

- Investigating breast cancer cell recruitment and survival in the bone niche using 3D-printed tissue-engineered bone models
- Over sees daily lab operations, ensures proper maintenance of equipment, supplies, and safety protocols
- Resolves experimental and technical issues to ensure the continuity and success of research activities

Research Assistant, SAFETY IMPACT Lab, Blacksburg, VA September 2022 – 2023

- Developed an R code to predict occupant rib fractures in passenger vehicle crashes from real-world crash data using Crash Investigation Sampling System (CISS)
- Extracted frontal crash data for Automatic Emergency Braking (AEB) and Vision Zero analysis
- Assisted in writing a roadside encroachment coding manual for the National Cooperative Highway Research Program (NCHRP 17-88, 22-26)

Engineering Aide II, Henrico County WRF, Henrico, VA May 2022 – August 2022

- Bench Rotation (Solids, NH3, Micro., Nutrients, COD, CBOD)
- Trained and certified in proper pipette use (Serological, Volumetric, Automatic)
- Performed Monthly Quality Control on lab instruments
- Followed lab protocols when handling biohazard materials
- Collected and analyzed county drinking water samples

Production Team Lead, Panera Bread, Henrico, VA June 2018 – 2022

- Increased customer base through customer service and quality work
- Trained a dozen production and service ambassador positions
- Performed excellent customer service practices in a fast-paced work environment

Cashier, Walmart, Henrico, VA July – August 2018

- Efficiently handled goods to customers and transported them into their vehicles
- Performed excellent customer service practices in a fast-paced work environment

Publication

E. A. Shangin, S. Choi, E. Hunt, Z. Bahranifard, E. Nguyen, C. J. Collins, A. R. Whittington, Dynamic Micromechanical Characterization of 3D Printed Bone In Vitro Models Manufactured via

Vat Photopolymerization. Adv. Funct. Mater. 2025, 2418547. https://doi.org/10.1002/adfm.202418547

L. Bangert, W. Armstrong, **E. A. Shangin**, R. S. Martin, A. N. Miller, L. E. Riexinger, A. A. Weaver, Predicting Distal Tibia Fracture Type using Demographic, Vehicle, and Crash Factors via a Random Forest Classification Algorithm. Traffic Inj. Prev. 2025. (In Submission)

L. E. Riexinger, H. C. Gabler, **E. A. Shangin**, M. Daanen, N. Pradeep, M. Dean, M. Bareiss, D. Gabauer, Roadside Encroachment Database Development and Analysis. NCHRP TRB-NRC. 2023 (In Submission)

Conference Oral Presentations & Posters

S. Choi, E. Hunt, **E. A. Shangin**, Z. Bahranifard, E. Nguyen, C. J. Collins, A. R. Whittington, Dynamic micromechanical characterization of 3D printed bone in vitro models manufactured via vat photopolymerization, SB3C 2024 Annual Meeting (Oral)

M. Roberts, D. S. Johnson, **E. A. Shangin**, K. Oyediran, S. Ferrao, C. J. Collins, Linking the Cancer Cell Glycocalyx and Lymphatics in Breast Cancer, Physical Sciences of Cancer Gordon Research Conference 2025 (Poster)

S. Choi, E. Hunt, **E. A. Shangin**, Z. Bahranifard, E. Nguyen, C. J. Collins, A. R. Whittington, Impact of Murine Cell Seeding on Vat Photopolymerized 3D Printed Scaffolds, Materials Science & Technology Symposium 2024 (Oral)

Shangin EA, Kleinschmidt K, Riexinger LE, Using Real-World Crash Data to Predict the Number of Occupant Rib Fractures, AAAM 67th 2023 Annual Meeting (Oral)

Honors & Awards

- NSF Graduate Research Fellowships Program Honorable Mention, Spring 2025
- Powell Fellowship, Fall 2024 – Spring 2025
- Dean's List at Virginia Tech, Spring 2022 – 2024
- Presidential Scholarship Initiative Scholar, Fall 2020 – 2024
- Clay Gabler Award of Excellence Scholar, Spring 2023
- C. Douglas Guess Memorial Scholarship Scholar, Fall 2020

Involvement & Outreach

- Collins Lab Tour, Spring 2025
- Volunteer for National Biomechanics Day, Spring 2024, Spring 2025
- Volunteer of Virginia Tech: Big Event, Spring 2025
- South Central TSA High School Judge, Spring 2024
- All Saints Episcopal Church Youth Mentor, Summer 2016 – Summer 2020
- Highland Springs High School TSA President, Fall – Spring 2020